

POLITECNICO DI TORINO

**Master of Science in
Energetic and Nuclear Engineering**

Master Thesis

Thermal-Fluid Dynamic Modelling of a Thermocline Storage System for CSP Applications



Tutors:

Prof. Roberto Zanino

Dr. Mattia Cagnoli

Candidate:

Ivan Pellegrino

S262658

a.y. 2019/2020

Un ringraziamento speciale va al Prof. Roberto Zanino e all'Ing. Mattia Cagnoli che mi hanno seguito durante tutto lo svolgimento di questa tesi. A quest'ultimo in particolare sono grato per avermi assiduamente supportato e guidato con puntualità, costanza, chiarezza, figlie di un'eccellenza sia dal punto di vista umano che da quello didattico.

Desidero poi porgere i miei più sentiti ringraziamenti a Walter Gaggioli, che mi ha accolto durante la permanenza al centro ENEA La Casaccia, e che con numerosi seminari mi ha permesso di ampliare le mie competenze nell'ambito di questa tesi, e non solo. Ringrazio altresì per la loro gentilezza e competenza, gli altri esponenti di ENEA: Valeria Russo, Raffaele Liberatore, Alberto Giaconia, che come Walter hanno generosamente dedicato ore del loro tempo al mio lavoro, mettendo a disposizione il materiale necessario e le loro conoscenze. Il loro interesse e la passione per la materia sono stati una forte fonte di ispirazione, sfociando in un confronto sempre fruttuoso e decisivo per il progredire del lavoro.

Ringrazio infine i miei familiari, grazie ai quali ho potuto dedicarmi a tempo pieno e con tutto me stesso a questo lavoro, e prima di esso al mio intero percorso di studi, con la serenità di chi sa che non gli sarà fatto mai mancare nulla.

Summary

| | |
|---|-----------|
| Acronyms..... | 9 |
| Abstract | 11 |
| Estratto in Italiano..... | 13 |
| 1. Introduction..... | 15 |
| 1.1 Decarbonisation of the Energy Sector | 15 |
| 1.1.1 Solar Technologies | 17 |
| 1.1.2 Critical aspects..... | 18 |
| 1.2 Concentrating Solar Power (CSP) Technology | 20 |
| 1.3 Thermal Energy Storage (TES) | 22 |
| 1.3.1 Double Tank Configuration..... | 23 |
| 1.3.2 Single Tank Configuration: Thermocline Storage..... | 25 |
| 2. Experimental Campaign | 29 |
| 2.1 Design of the Thermocline TES | 30 |
| 2.1.1 Main Components | 30 |
| 2.1.2 Materials | 34 |
| 2.1.3 Working Principle | 35 |
| 2.2 Description of the Testing Facility | 37 |
| 2.2.1 Testing Circuit | 37 |

| | |
|---|-----------|
| 2.2.2 Measuring Instrumentations | 38 |
| 2.3 Experimental Data | 39 |
| 2.3.1 Discharge Tests | 40 |
| 2.3.2 Charge Tests | 42 |
| 2.3.3 No-Load Test..... | 43 |
| 3. Development of the CFD Model | 45 |
| 3.1 Choice of the Model Dimensionality | 45 |
| 3.2 Definition of the Computational Domain | 47 |
| 3.2.1 Simplification of the Minor Components..... | 47 |
| 3.2.2 Impeller..... | 49 |
| 3.2.3 Resulting Computational Domain | 49 |
| 3.3 Boundary Conditions | 51 |
| 3.3.1 Heat Exchangers: Heat Load | 51 |
| 3.3.2 Convective Thermal Losses..... | 54 |
| 3.3.3 Advective Thermal Losses | 56 |
| 3.3.4 Initial Conditions | 56 |
| 3.4 Main Features of the Model..... | 57 |
| 3.5 Definition of the Computational Mesh | 58 |
| 3.5.1 Characteristics of the Mesh | 58 |
| 3.5.2 Mesh Independence Study..... | 59 |
| 3.5.3 Timestep Independence Study..... | 62 |
| 3.6 Calibration of the Thermal Losses..... | 63 |
| 3.7 Benchmark | 65 |
| 3.7.1 U-Shaped Tube with Analytical Equivalent..... | 65 |

| | |
|---|-----------|
| 3.7.2 Verification Against Experimentally Verified Data | 67 |
| 3.7.3 ENEA Preliminary CFD Model | 68 |
| 4. Validation of the Model..... | 69 |
| 4.1 Comparison with Experimental Data..... | 69 |
| 4.2 Analysis of the Problem..... | 72 |
| 4.3 Modification of the Geometry | 75 |
| 4.3.1 Parametric Analysis on the Bypass Thickness | 76 |
| 4.3.2 Final Model | 78 |
| 4.4 Validation of the Final Model..... | 79 |
| 4.4.1 Charge test 2 | 79 |
| 4.4.2 Discharge test 4: selected transient..... | 83 |
| 5. Conclusions and Perspective..... | 87 |
| Appendices..... | 89 |
| Appendix A..... | 89 |
| Impeller Bidimensional Axisymmetric Representation | 89 |
| Appendix B | 91 |
| Thermophysical Properties of the Materials..... | 91 |
| Appendix C | 94 |
| Other Results: Charge Test 1.1 | 94 |
| Other Results: Charge Test 1.2..... | 95 |
| Other Results: Discharge Test 4 | 96 |
| Other Results: Discharge Test 6 | 97 |
| References..... | 99 |

Acronyms

| | |
|--------------|------------------------------|
| BC(s) | Boundary condition(s) |
| CFD | Computational Fluid Dynamics |
| CSP | Concentrating Solar Power |
| GHG | Greenhouse Gases |
| HSM | Heat Storage Medium |
| HTC | Heat Transfer Coefficient |
| HTF | Heat Transfer Fluid |
| HX(s) | Heat Exchanger(s) |
| IC(s) | Initial Condition(s) |
| MS | Molten Salts |
| RES | Renewable Energy Sources |
| TES | Thermal Energy Storage |

Abstract

The objective of this work is the development of a CFD model able to reproduce the transient behaviour of the prototype of a molten salts thermocline energy storage with two integrated heat exchangers connected by an internal channel, designed by ENEA (*Italian institute for new technologies, energy and sustainable development*) for CSP applications.

Firstly, a brief introduction to the general topic of *decarbonisation of the energy sector* and the increasing importance of low carbon technologies in the present and future developments of energy production is given. A particular focus is set on the topic of CSP and *sensible thermal storage*.

Afterwards, an exhaustive description of the idea behind the design of the prototype and its working principle is provided to the reader, alongside with the characteristics of the experimental setup in terms of materials involved, testing circuit topology, measuring instrumentations installed and experimental data available.

The CFD modelling is performed using the commercial code *Simcenter STAR-CCM+* by Siemens, together with the commercial software *SolidWorks*® by Dassault Systèmes, used for the creation of the CAD reproduction of the facility under study. The chosen computational domain is a bidimensional axisymmetric representation of the storage, that enables to obtain accurate results with a reduced computational cost. But, in order to obtain this symmetry, some minor components are not included in the domain, requiring a calibration of the model in order to match the experimental thermal losses towards the environment, accounted for through constant Robin boundary conditions on the external surfaces of the computational domain. Instead, the heat load that is applied on the tank by the diathermic oil flowing inside the heat exchangers, is initially reproduced by means of

a time variable Robin boundary condition, in accordance with the experimental data. The characteristics of the computational spatial and temporal mesh are presented: they are chosen thanks to a mesh independence study, with a mesh that is more refined in fluid regions, especially where the temperature and velocity gradients are more important, like on the heat exchangers external walls. Finally, the specific models applied are listed, and their capability to accurately reproduce buoyancy driven phenomena is verified with some benchmark simulations.

A first comparison with the experimental data shows an important difference between the outcome of the CFD simulations and the experiments, in particular regarding the salts motion inside the internal channel, strongly underestimated by the model. One possible cause of this problem is shown to be the presence of a bypass in parallel to the heat exchangers, that allows a much higher molten salts motion. This is believed to be a possible option provided that the final drawings of the prototype are not available. A possible configuration of this bypass is presented, and its thickness determined through a parametric analysis. The design geometry initially implemented in the model is modified accordingly, and the heat load boundary condition simplified into a simple heat source, imposing the experimental heat load. Finally, the results of the simulations with this new configuration are compared to some experimental charge and discharge transients, obtaining a satisfactory accordance, hence validating the model.

Estratto in Italiano

L'obiettivo di questo lavoro è lo sviluppo di un modello CFD in grado di riprodurre il comportamento in transitorio del prototipo di serbatoio termoclino di stoccaggio di energia termica, dotato di due scambiatori di calore integrati connessi da un canale interno, progettato da ENEA (*Agenzia nazionale per le nuove tecnologie l'energia e lo sviluppo economico sostenibile*) per applicazioni CSP.

In primo luogo, viene fornita una breve introduzione generale riguardo la *decarbonizzazione del comparto energetico* e la crescente importanza delle tecnologie a basso tenore di carbonio negli sviluppi presenti e futuri della produzione di energia. Un'attenzione particolare è riservata agli argomenti del solare a concentrazione e delle tecnologie di stoccaggio basate su calore sensibile.

Dopodiché, viene fornita al lettore una descrizione esaustiva dell'idea dietro al design del prototipo e al suo principio di funzionamento, insieme alle caratteristiche dell'apparato sperimentale in termini di materiali, topologia del circuito, strumentazioni di misura installate e dati sperimentali disponibili.

La modellazione CFD è effettuata usando il software commerciale *Simcenter STAR-CCM+* di Siemens, insieme con il software commerciale *SolidWorks*[®] di Dassault Systèmes, usato per la creazione della riproduzione CAD dell'impianto studiato. Il dominio computazionale scelto è una rappresentazione bidimensionale assialsimmetrica del serbatoio, che permette di ottenere risultati accurati riducendo i tempi di calcolo. Però, per ottenere questa simmetria, alcuni componenti minori non sono stati inclusi nel dominio, richiedendo una calibrazione del modello affinché potessero essere riprodotte correttamente le perdite termiche verso l'ambiente verificate sperimentalmente, tenute in conto per mezzo di condizioni al contorno di tipo Robin, costanti, applicate sulle pareti

esterne del dominio di calcolo. Invece, il carico termico, che è applicato al serbatoio dall'olio diatermico che scorre all'interno degli scambiatori di calore, è inizialmente riprodotto per mezzo di una condizione al contorno di tipo Robin, variabile nel tempo in accordo ai dati sperimentali. Vengono presentate poi le caratteristiche della griglia di calcolo, spaziale e temporale: sono scelte attraverso uno studio di indipendenza dei risultati dalla griglia, con una mesh più rifinita nelle regioni fluide, specialmente dove i gradienti termici e di velocità sono più importanti, come sulle pareti esterne degli scambiatori di calore. Infine, sono elencati i modelli applicati nello specifico, e la loro capacità di riprodurre accuratamente fenomeni la cui forzante principale sono le forze di galleggiamento, è verificata con delle simulazioni di riferimento.

Un primo confronto con i dati sperimentali mostra una consistente differenza tra i risultati delle simulazioni CFD e gli esperimenti, in particolare riguardo al movimento di sali all'interno del canale, fortemente sottostimato dal modello. Una possibile causa di questo problema, viene dimostrato essere la presenza di un bypass in parallelo agli scambiatori di calore, che permette una movimentazione di sali molto maggiore. Questa è ritenuta un'opzione plausibile in quanto i disegni costruttivi del prototipo non risultano disponibili. È presentata poi una possibile conformazione di questo bypass, il cui spessore viene determinato attraverso un'analisi parametrica. In accordo con ciò, la geometria di progetto, inizialmente implementata nel modello, viene quindi modificata, e la condizione al contorno per la definizione del carico termico è semplificata, diventando semplicemente una fonte di calore la cui grandezza è quella determinata sperimentalmente. Infine, i risultati delle simulazioni con questa nuova configurazione vengono confrontati con alcuni dei transitori sperimentali di carica e scarica, ottenendo un accordo soddisfacente e quindi validando il modello.

Chapter 1

1. Introduction

The objective of this work is the development of a *Computational Fluid Dynamics (CFD) model*, able to reproduce the transient charging and discharging phases of the testing prototype of an innovative concept of *molten salts thermocline energy storage with integrated heat exchangers* for *Concentrating Solar Power (CSP)* applications, designed by ENEA (*Agenzia nazionale per le nuove tecnologie l'energia e lo sviluppo economico sostenibile – Italian institute for new technologies, energy and sustainable development*) in the framework of the European Project *ORC-PLUS* [1].

In this chapter, some background information is provided on the reasons that suggest the CSP technology, coupled with thermal energy storage technologies, as an important option for the future of the energy production.

1.1 Decarbonisation of the Energy Sector

The phenomenon of *Global Warming* is very well known. It can be defined as the increase of the global average temperature of our planet, mainly due to the *Greenhouse effect*, enhanced by the increasing anthropogenic emissions of the so-called *Greenhouse Gases (GHG)*, such as carbon dioxide and methane [2]. An important percentage of these anthropogenic emissions is related to energy production, considering that the 81% of the *world primary energy demand* was still satisfied by fossil fuels in 2017 [3].

The necessity of mitigating this phenomenon is very well known as well. In 2015, with the *Paris Agreement*, the United Nations Framework Convention on Climate Change (UNFCCC) officially ratified that “*holding the increase in the global average temperature to well below 2°C above pre-industrial levels [...] would significantly reduce the risks and impact of climate change*”. In order to comply this condition, as outlined by the International Energy Agency (IEA) in the *sustainable development scenario* [3] and illustrated in **Figure 1.1**, the amount of GHG emissions from power production using fossil fuels needs to be drastically reduced in the near future. To do so, improvements in the energy production and utilization processes, a further penetration of technologies based on *Renewable Energy Sources* (RES), alongside with *Nuclear Power* and the innovative *Carbon Capture Utilisation and Storage* (CCUS) technologies, are necessary [2].

In particular, those technologies that rely on renewable sources such as wind, sun, water and biomass for the production of energy, are having an essential role in this energy transition [4]. Wind and water are exploited basically to rotate a turbine and directly produce electricity, while the sun is exploited in different ways.

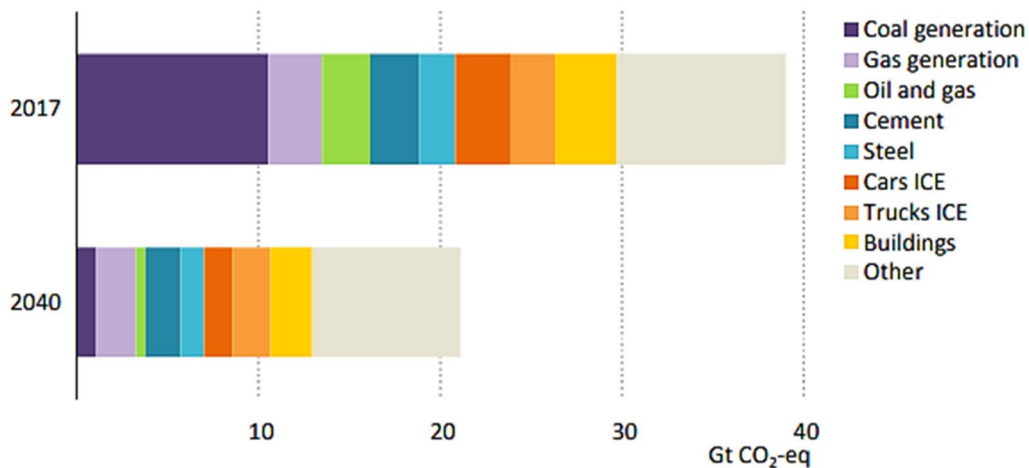


Figure 1.1 GHG emissions from selected sectors (2017) and in the Sustainable Development Scenario (2040) [3]

1.1.1 Solar Technologies

Every year, 3,400,000 EJ of solar radiation reach the surface of the earth, that is more than 7,500 times the total annual primary energy consumption registered in 2013 [5]. The potential of the solar resource is huge, and it can be exploited in different ways to produce either electricity, heat, or even a combination of them. *Solar Thermal* technologies exploit the direct solar radiation in order to heat up a heat transfer fluid (HTF) flowing in pipes inside a solar collector, typically water (or water + glycol) used for the production of domestic hot water in rooftop applications at a residential scale. On the other hand, *solar photovoltaic (PV)* technologies exploit the properties of semiconductors that, if properly assembled forming a p-n junction, can directly generate a coherent flux of electrons when hit by solar radiation, and then useful electricity using solar panels made out of electrically connected cells. A strong drawback of this technology is represented by the fact that the solar resource is strongly time dependent (available only during the day), and unpredictable: coupling with batteries is then the only solution for making this electricity dispatchable. Finally, *Concentrating Solar Power (CSP)* uses concentrated solar radiation to heat up an HTF, that is then exploited to drive a thermodynamic cycle (typically a Rankine cycle) for electricity production. The main advantage of this technology is the possibility of storing the thermal energy or even use it for district or industrial heating applications. More details about CSP are given in *section 1.2*.

The spread of these technologies is experiencing its most florid historical period, provided that the global renewable capacity has grown more and more every year in the last 15 years, and this trend is expected to be confirmed in the next future. This is shown in **Figure 1.2**, where the prominent role of solar photovoltaic (PV), but also of wind power, above the other renewable technologies in terms of new installations appears clear.

According to the forecasts, in 2024 the share of power generated with renewable technologies will be of about 30% [4], and it is hopefully going to furtherly increase up to a very consistent percentage in the next decades. Nonetheless, as some communities with

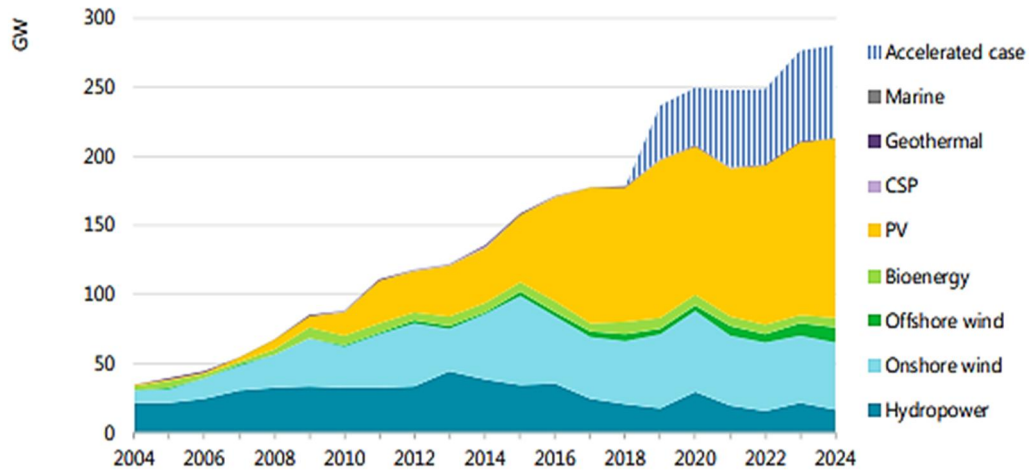


Figure 1.2 Annual renewable capacity addition by technology, main and accelerated case [4]

a very high RES penetration (especially PV, like in California [6]) are already experiencing, such a radical modification in the energy production paradigm is not straightforward, since a rapid growth in the share of renewables in the energy mix creates some critical issues in the management of the grid.

1.1.2 Critical aspects

RES are mostly not continuous and unpredictable. The grid cannot rely on solar PV and wind power plants alone in order to match the demand, but some *base-load plants* are still necessary. Base load plants must work almost continuously and need to produce electricity at a very low cost. The battery technology is not mature enough to allow large electricity storage for PV and wind power plants at a competitive cost (**Figure 1.3**). Therefore, given the low acceptability of nuclear power plants by the population, and provided that hydroelectric power is already strongly exploited and sites for new installations are hardly available, in most of the cases the base-load has still to be satisfied by the most carbon intensive coal fired power plants [7].

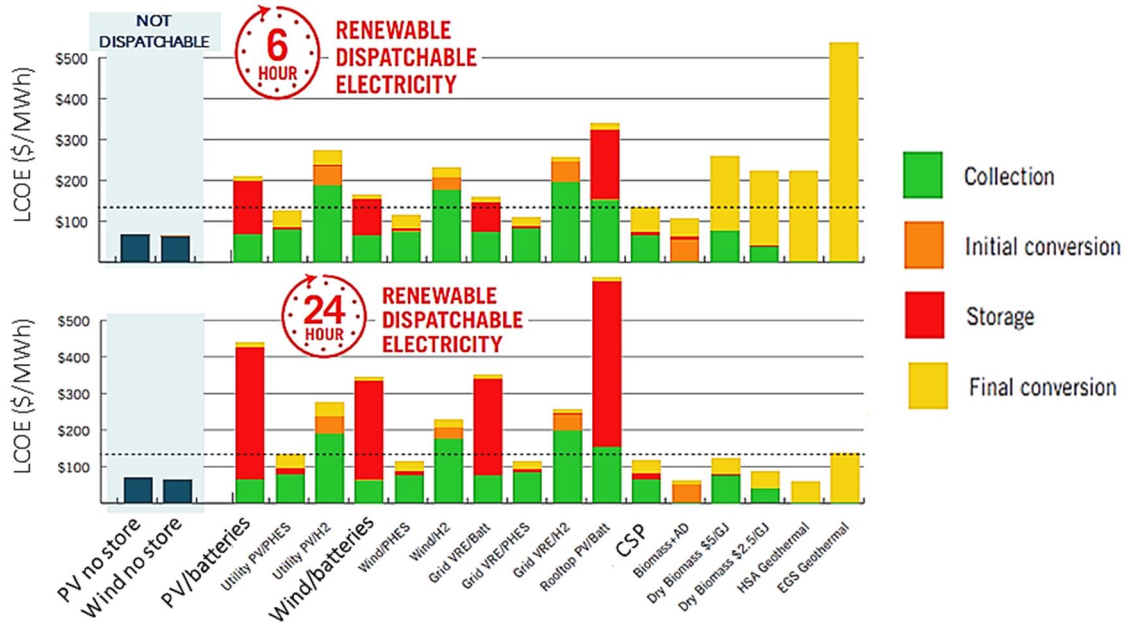


Figure 1.3 Levelized Cost of Electricity (LCOE) comparison for different technologies and different storage durations [36]

Other big concerns specifically regard PV penetration, namely the risk of *overgeneration* and the management of the so-called *evening ramp* [6]. They can both be clearly shown and summarized by the *Duck Curve* represented in **Figure 1.4**. In fact, the risk of overgeneration leads to the need for *curtailment* of the non-dispatchable PV generation in the central hours of the day (i.e. make the plants produce less than they would have normally done), when the production overcomes the demand and conventional base-load plants cannot be further backed down. Furthermore, the evening ramp issue is at least as critical as the previous one: solar PV stops producing at sunset exactly in correspondence with the usual evening peak of the demand, causing a very steep upward ramp in the power that must be supplied by conventional generation plants, the (more or less) slow starting transients of which must be carefully taken into account.

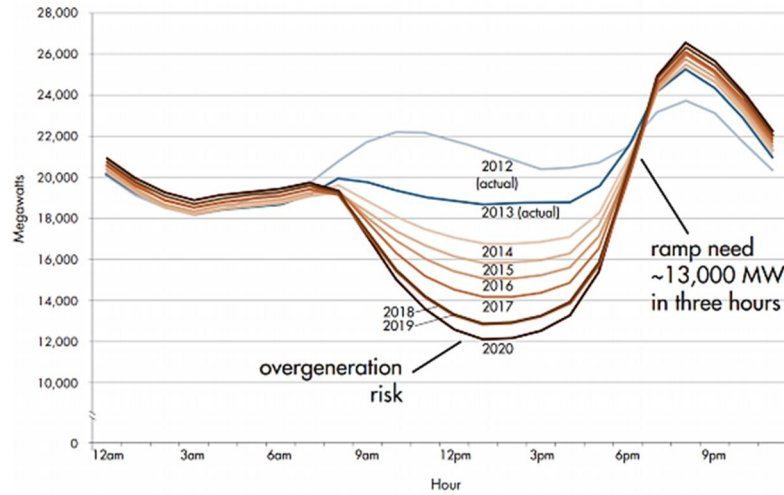


Figure 1.4 Predicted "Duck Curve" evolution in California [6]

Several *Demand-Side Management* approaches are useful for reducing these problems [8]. On the side of *supply* instead, CSP can have a crucial role: immediately, given the cost competitiveness in the coupling with storage (**Figure 1.3**) and as already planned for instance in the ORC-PLUS project, it can be effectively used for switching the production from solar source later in the evening, when the peak usually occurs and the ramp urges, flattening the curve and reducing the pressure on conventional plants [9]; moreover, given the low costs of the CSP/storage configuration, a fraction of the conventional base-load plants could be potentially replaced by a renewable source of dispatchable energy. The characteristics of this promising technology are then presented in the next section.

1.2 Concentrating Solar Power (CSP) Technology

A CSP plant is also called *solar thermal power system*, since it basically exploits the solar radiation in order to heat up a fluid at a suitable temperature to run a *conventional thermodynamic cycle* for power production. For this purpose, the solar radiation, which is about 1 kW/m^2 at ground level, has to be concentrated in order to reach high heat fluxes.

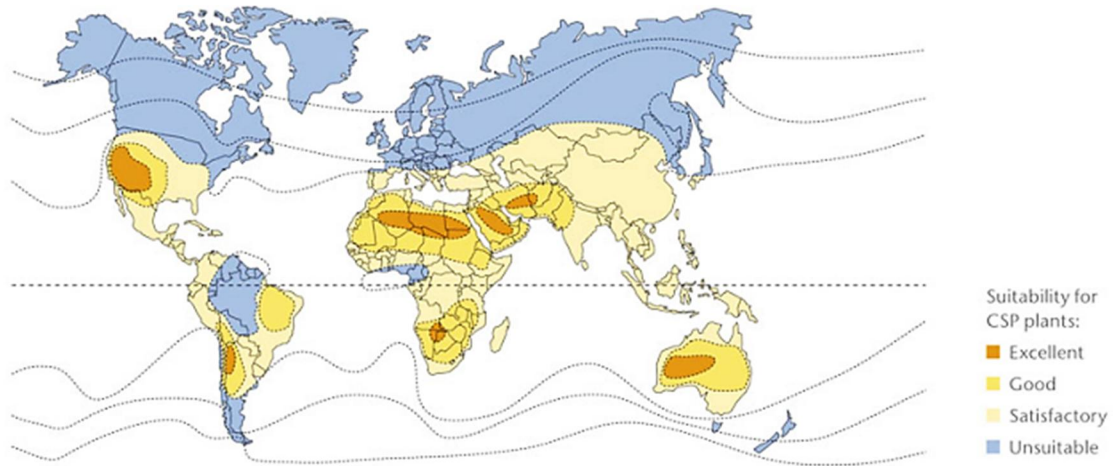


Figure 1.5 Worldwide suitability map for CSP technology [37]

The concentration is the most important aspect when talking about a CSP plant: how the concentration is performed characterizes the plant as a whole, in terms of temperatures, efficiency, costs, materials and power cycle. There are two concentrating options: *line-focusing* systems (parabolic trough and linear Fresnel) that can concentrate the sunlight by one hundred times, and *point-focusing* systems (central tower systems and dish concentrators), up to several thousands [10]. Despite these different possibilities, concentration is in any cases performed by mirrors reflecting the radiation coming directly from the sun, so that best locations for a CSP plant are characterized by a low latitude (the so-called *sun belt* around the equator), by a high number of clear sky days and by low levels of humidity and air pollution. Hence, the suitability of a location for the installation of a CSP plant (**Figure 1.5**) can be synthesized in a parameter called *Direct Normal Irradiation* (DNI), that represents the energy per unit surface that reaches directly the earth for every year. In particular, at least $2000 \text{ kWh/m}^2/\text{y}$ are required for plant profitability at the state of the art, while the best sites are irradiated by $2800 \text{ kWh/m}^2/\text{y}$ [11]. Considering that the 61% of the 5 GW globally installed in 2015 were in Spain, which is not among the very best locations in terms of DNI, the potential growth of this technology in the future appears clear.

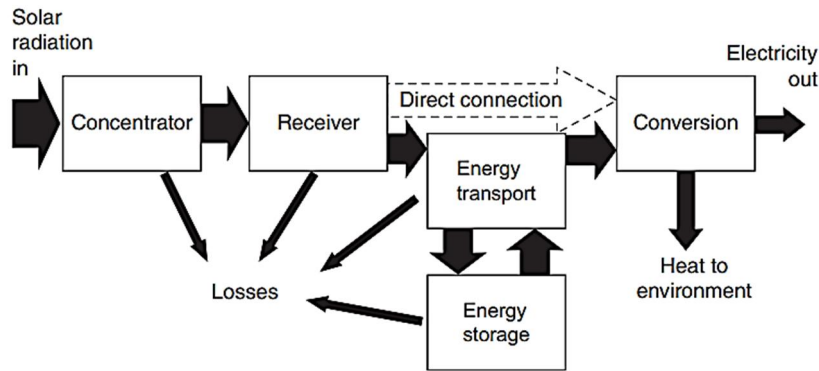


Figure 1.6 Schematic representation of the components of a CSP plant [10]

The main components of a CSP plant and their functional connections are shown in **Figure 1.6**. In particular, regarding the *conversion* of the thermal energy into electrical energy, conventional power blocks are often coupled to line-focusing systems, in particular *steam Rankine cycles* or *Organic Rankine Cycles (ORC-PLUS project [1])* for lower temperature levels. On the other hand, point-focusing systems can be coupled with Stirling engines (dish concentrators) or Brayton cycles (both dish and central tower systems). Eventually, since the thesis work is developed within the subject of *thermal energy storage*, this topic is presented with some more details in its own *section 1.3*.

1.3 Thermal Energy Storage (TES)

As already suggested in *section 1.1.2*, the possibility of storing the thermal energy collected by the solar field is probably the most appealing feature of this technology, since it allows the plant to produce dispatchable power, i.e., even when the sun is absent the CSP plant is able to generate electricity, unlike PV or wind plants without batteries. The design and sizing of the storage determines the task of the plant, so that one can distinguish between *peaker designed power plants*, that collect the energy of the sun and discharge during the evening or even morning peak, and *base-load designed power plants*, that should be very stable and reliable, ensuring a 24/7 production [11]. The size of the storage is usually expressed using a parameter called *storage hours (SH)*, defined

as the ratio between the storage energy capacity Q_{stor} and the thermal energy necessary in order to run the power block for 1 h at nominal power P_{nom} , given a storage-to-electricity efficiency η_{st-el} :

$$SH = \frac{Q_{stor}}{1h \times P_{nom}/\eta_{st-el}} \quad (1.1)$$

Now, the most delicate aspect is the needed storage capacity: for instance, 1 GW_{th} of capacity are approximately necessary in order to obtain $SH = 7$ for a 50 MW_{el} parabolic trough plant. Consequently, provided that many options could be in perspective available such as steam accumulators and thermochemical or latent heat storage using various kinds of *phase changing materials* (PCM), but still at the state of the art *sensible heat storage* remains the most used solution [10], then one of the most critical aspects when dealing with the costs of a thermal storage system is the huge amount of *heat storage medium* (HSM) that is required. In fact, for a sensible heat storage the necessary quantity of HSM m_{HSM} is directly proportional to the storage capacity through the equation:

$$Q_{stor} = m_{HSM} \int_{T_{min}}^{T_{max}} c_{HSM}(T) dT \quad (1.2)$$

where $c_{HSM}(T)$ is the *specific heat* of the material. Hence, it is easy to understand that the major contribution to the cost of a thermal storage system (that accounts for a percentage ranging between 10% and 20% of the total cost of a CSP plant [12]), is given by the purchasing of the heat storage material.

The main sensible heat storage solutions are now presented.

1.3.1 Double Tank Configuration

It is the most common configuration, with two tanks named *hot tank* and *cold tank*, containing respectively the highest and lowest temperature HSM. At the state of the art

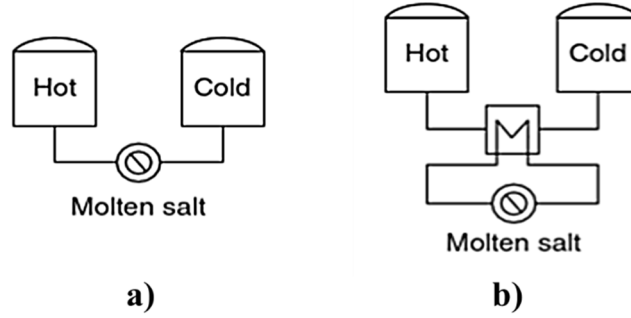


Figure 1.7 a) Direct and b) Indirect two tank thermal storage configuration [10]

the medium is typically a eutectic mixture of nitrate salts (60% NaNO_3 and 40% KNO_3 in weight) named *Solar Salt*, and two different setups are possible: *direct* and *indirect* storage (**Figure 1.7**). The latter is more common, and consists of two different circuits, one for the heat transfer fluid, that is usually a thermal oil, and heats up through a heat exchanger the cold salts flowing in the other one and directed towards the hot tank. The advantage of this option is the relatively low cost of the components of the oil circuit, whilst as a drawback the highest temperature is limited to around 390°C by the thermal oil maximum temperature ($\sim 400^\circ\text{C}$) and the pinch point at the oil/salts heat exchanger. As a consequence, calling this temperature T_{max} and considering that the lowest temperature T_{min} is limited by the freezing point of the salts mixture (238°C [13]) and it is typically set to 290°C , we can conclude on the base of **equation (1.2)** that a higher temperature difference would allow to store the same amount of energy with a smaller quantity of HSM. This goal is reached by using the *direct* configuration, in which only one circuit remains, the solar salts are used as both HTF and HSM, and it is possible to achieve hot temperatures of almost 600°C with central tower systems (above which unbearable corrosion of the components would take place [13]) and of around 540°C with parabolic troughs. As a drawback, part of the cost reduction due to the smaller amount of HSM needed, is counterbalanced by the higher cost of the high-quality circuit components for higher temperatures and salts corrosion.

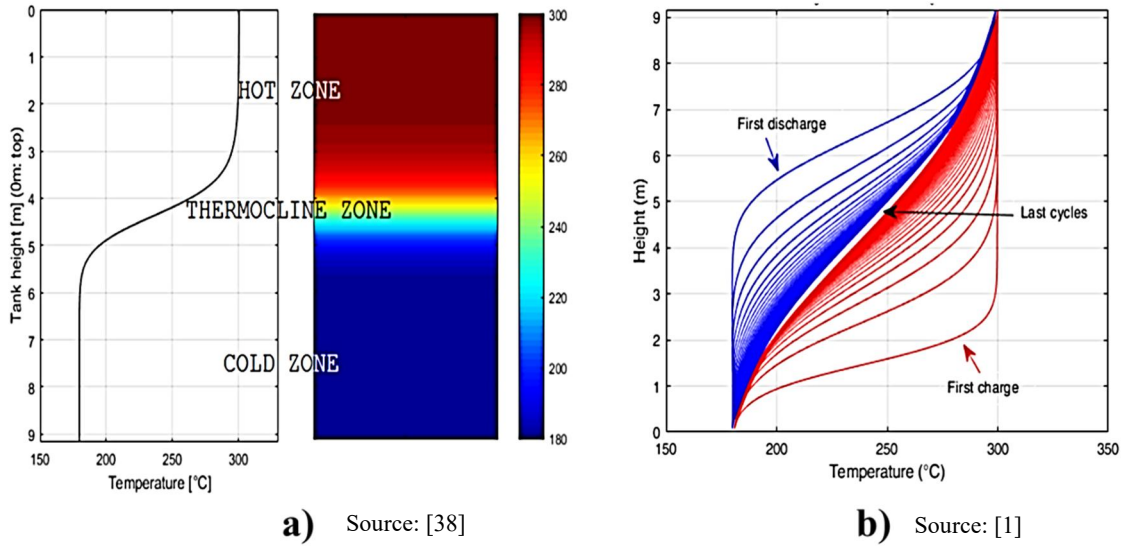


Figure 1.8 a) Schematic representation of the thermocline inside a tank and b) Thermocline Hysteresis

1.3.2 Single Tank Configuration: Thermocline Storage

The possibility of using only one tank allows to simplify the plant, to reduce the number of components and then to potentially reduce the overall plant cost. Using a concrete storage would be by far the cheapest solution (10÷20% of the corresponding cost for molten salts [10]), ensuring an acceptable heat capacity. Some pilot plants have already been ran [14], but the problems regarding the very low thermal conductivity of the material and its resistance to thermal cycling are still under investigation (e.g. [15]).

The other option for a single tank configuration are the *thermocline storage*, in which both the hot and the cold fluid are contained in the same tank, separated by thermal stratification due to buoyancy forces, with an intermediate zone called thermocline, where the temperature gradient occurs (**Figure 1.8a**). These are systems that could strongly reduce the storage cost with respect to the two tanks counterpart, but that require a very accurate design and operation control in order to work effectively. The main concern is to avoid the phenomenon called *hysteresis*, namely the progressive degradation of the thermocline after many cycles of operation (**Figure 1.8b**). In fact the ideal condition one would like to keep, is those that mimics the two tanks configuration, in which the hot and the cold

fluid are perfectly separated, and the thermocline thickness is null [16]. The reason for this is clearly explained by Rosen [17], who highlights how the **efficiency of a thermocline storage** should be correctly assessed using *exergy analysis* in addition to *energy analysis*. In effect, through an energy analysis it is straightforward to evaluate the energy losses (that are not a very big concern indeed, since thermal insulation towards the environment is relatively cheap and easy to be applied), whilst the main problem to be accounted for, according to Rosen, is the *degradation of the stored energy*, also called *loss of stratification*, evaluable through an exergy analysis. As a demonstration, considering a thermocline TES with fixed extreme temperatures T_{min} and T_{max} and a given amount of stored energy, each temperature profile different (i.e. less stratified) from the ideal one (i.e. one layer at T_{max} , one layer at T_{min} , perfectly separated), could be potentially obtained through an adiabatic mixing of the ideal layers, and it is well known that the exergy destruction (i.e. the energy degradation) due to the mixing of two fluids at different temperatures is always positive. So, practically speaking, the thinner is the thermocline, the closer is the behaviour of the storage to the ideality.

Four primary contributions to the degradation of the stored energy are identified in the paper:

- ❖ heat losses to (or leakages from) the surrounding environment;
- ❖ heat conduction from the hot portions of the storage fluid to colder portions;
- ❖ vertical conduction in the tank wall;
- ❖ mixing during charging and discharging periods.

Since the last item generally gives the major contribution, a lot of attention is given in many works to the design of the HSM *distributors* in order to minimize turbulences that would enhance this mixing, especially in direct storage, when the fresh HSM is poured into the tank (e.g. [18]). Another technological solution adopted for improving the stratification and for stabilizing the thermocline is the implementation of a filler material within the tank (e.g. quartzite rock [10], magnetite [1]), forming the so-called *packed bed thermocline energy storage*.

Beside these, an innovative design solution proposed and patented by ENEA for enhancing the thermal stratification consists in the integration of the heat exchanger(s)

inside the thermocline storage [19, 20]. This proved to be a good solution also because it offers the opportunity to simplify the circuit, furtherly reduce the number of components and then the costs. Different configurations of this design have been proposed and successfully tested in the last years, namely:

- ❖ a direct molten salts storage with integrated steam generator [19] (**Figure 1.9**);
- ❖ an indirect molten salts storage (using oil as HTF) with two spiral charging and discharging heat exchangers hosted in two separated channels [21, 22] (**Figure 1.10**);
- ❖ an indirect molten salts storage (using oil as HTF) with two conical coils heat exchangers contained in a single internal channel.

The latter is the subject of this thesis work, which will be accurately presented in the next chapter.

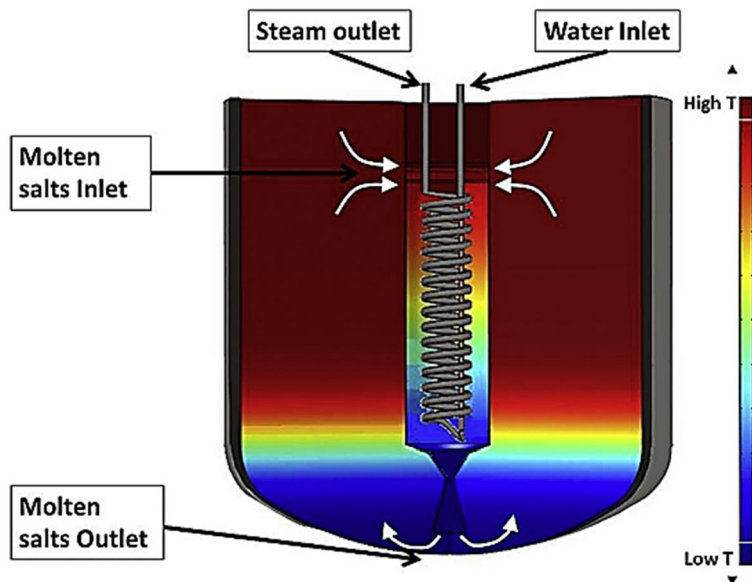


Figure 1.9 Schematics of Storage Tank with Integrated Steam Generator (STISG) by ENEA [39]

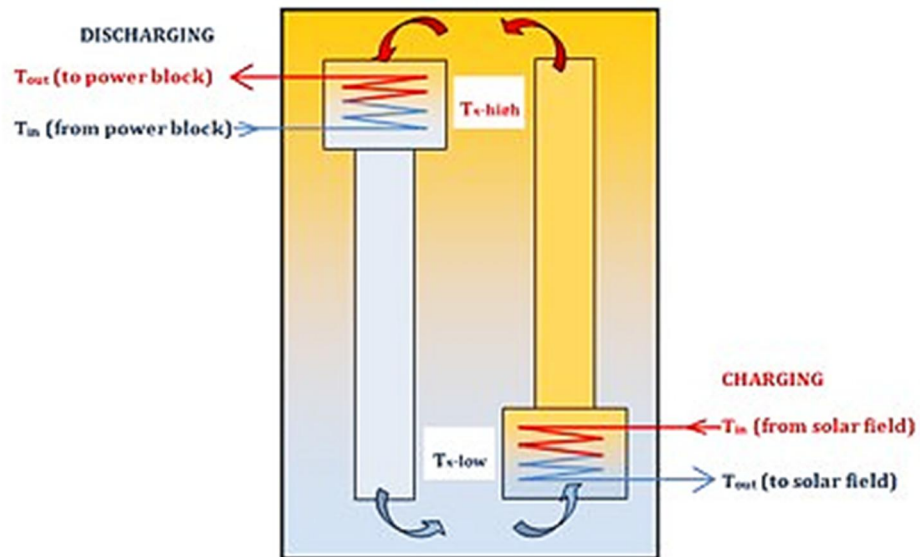


Figure 1.10 Two channels thermocline molten salts storage by ENEA [22]

Chapter 2

2. Experimental Campaign

The design of the molten salts storage that is going to be studied in this work was ideated by ENEA in the framework of the ORC-PLUS (Organic Rankine Cycle – Prototype Link to Unit Storage) European Project [1], in which the installation of a 20 MWh_{th} single tank TES in an existent plant in Benguerir (Morocco) was foreseen. It should have been linked with a newly installed linear Fresnel solar field using a mineral oil as HTF, with the task of ensuring at least 4 hours of additional production to a 1 MW_e ORC turbine during sunless periods (e.g. at sunset, correspondingly to the evening peak). Alongside with the design, ENEA presented a preliminary one dimensional finite differences numerical model in order to evaluate the behaviour of the tank in different operating conditions [23]. In addition, a 200 kWh_{th} testing prototype (scale 1:100) was installed at the *Casaccia Research Center (Rome, Italy)*, for the experimental validation of the feasibility of the innovative thermocline technology concept [24].

Although a packed bed thermocline storage with a magnetite filler was finally adopted in the ORC-PLUS Project, the ENEA Thermocline concept is a very promising and cost-effective solution to be used in small-medium scale CSP plants. Then, the development of a CFD model will allow, at first, to have a deeper understanding of how this thermocline prototype really works, and secondly to have a validated model to estimate the effectiveness of possible design improvements.

In the following sections, besides the design and working principle of the tank, the characteristics of the testing circuit and of the experimental data will be also presented.

2.1 Design of the Thermocline TES

The prototype is a cylindrical tank, with a diameter of 1300 mm, filled up with molten salts until a height of 2471 mm, for a storing capacity of 200 kWh_{th}, cycling between 180°C and 300°C. It works at atmospheric conditions and hosts also the internal channel with integrated heat exchangers, that is the core of the concept. Referring to *Figure 2.1*, the main components are listed, with their characteristics and materials.

2.1.1 Main Components

- ❖ **Charge Heat Exchanger:** it consists of 4 parallel serpentes (Ø 9.525 mm) with a conical coil evolution (aperture angle 140°) and 28 loops each, in which flows the hot diathermic oil coming from the solar field. It is located at the tank bottom, where the salts temperature is the lowest due to the thermal stratification. An explicative 3D view can be found in *Figure 2.2*.
- ❖ **Discharge Heat Exchanger:** it consists of 6 parallel serpentes (Ø 9.525 mm) with conical coil evolution and 28 loops each. Here flows the cold diathermic oil that brings the heat to the ORC cycle. Two more coils are added in the discharge HX since a higher discharge power is needed in order to use in four evening hours the amount of energy collected during the whole daytime through the charge HX. It is located at the tank top, where the salts temperature is the highest due to the thermal stratification.
- ❖ **Internal Channel:** it is a Ø 4"/102 mm tube lying on the tank axis, with the two extreme sides having a conical shape in order to host the heat exchangers (*Figure 2.2*). The molten salts move from the bottom to the top (charge phase) and vice versa (discharge phase) flowing in the channel. This allows enhancing the thermal stratification in the storage since the channel is thermally insulated and, therefore, the movement of the heated (or cooled) salts does not perturb the salts temperature stratification.

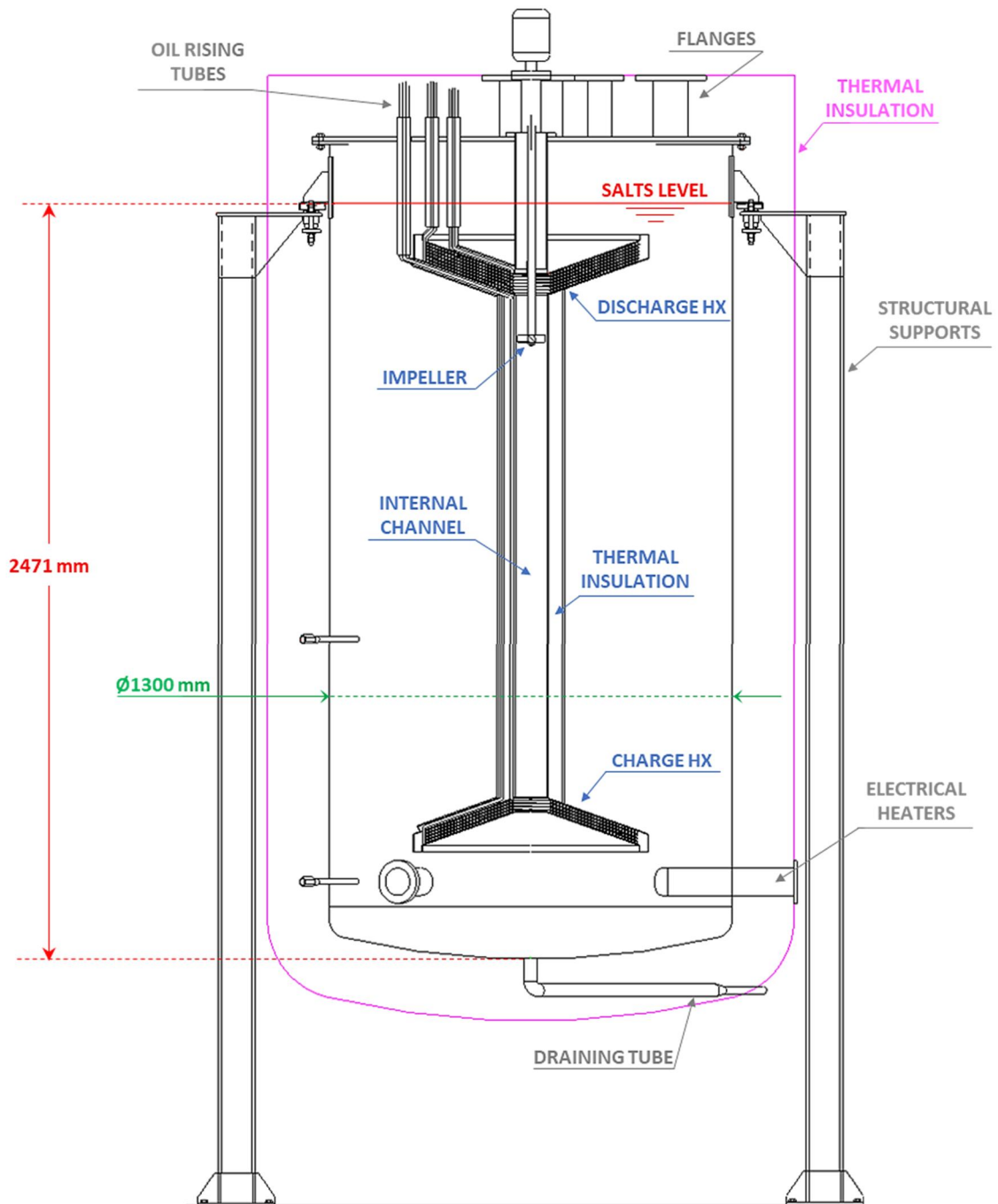


Figure 2.1 Thermocline TES scheme: main components

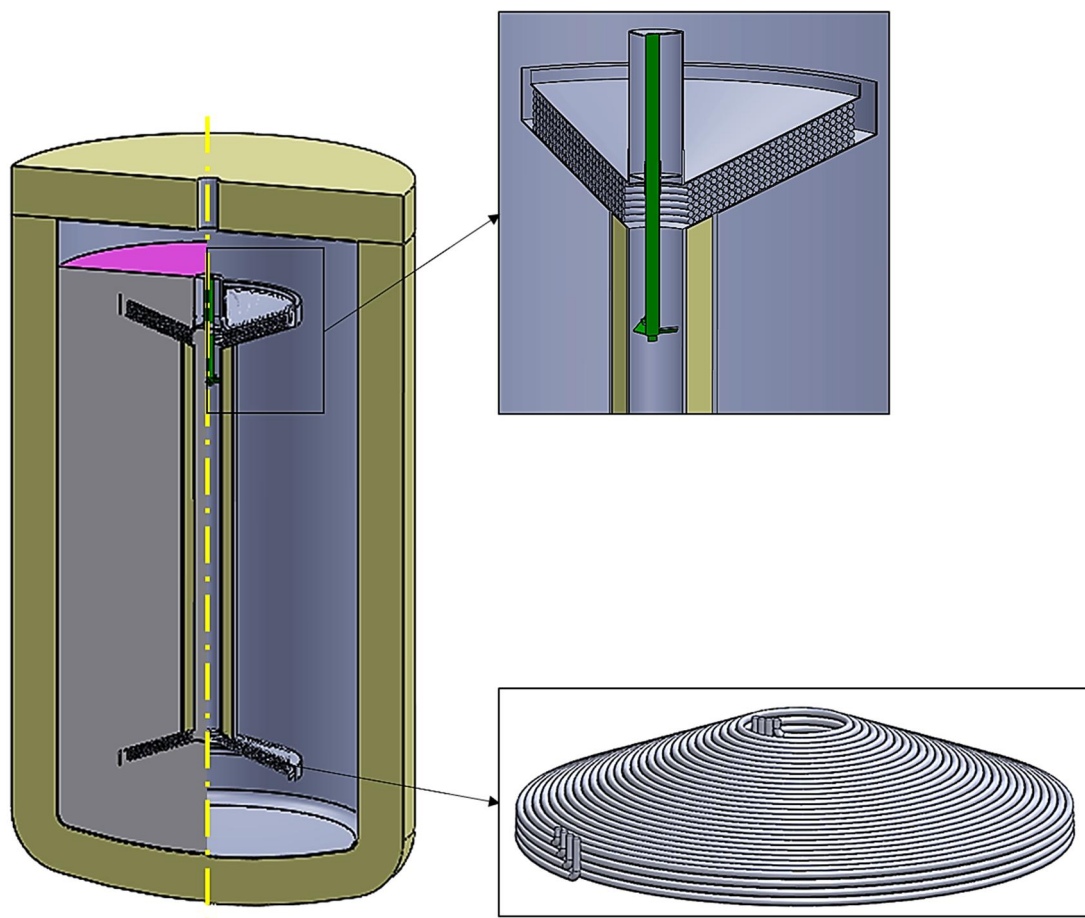


Figure 2.2 Tri-dimensional rendering of the main structure of the tank and details on HX and internal channel

- ❖ **Impeller:** it is a shaft equipped with 4 blades inclined at 45° . It is driven by its own motor and can rotate in both directions, with the objective of regulating the flux of molten salts in the channel during the operation. Unfortunately, the impeller behaviour during the experimental campaign was not satisfactory, as it is explained in *section 2.3*.

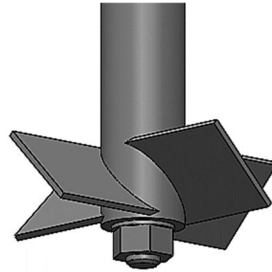


Figure 2.3 3D view of the impeller

- ❖ **Oil rising tubes:** they are necessary for the diathermic oil to reach either the discharge or the charge heat exchanger and come back out, from the tank top. They are thermally insulated, wherever possible. In particular, the charge rising tubes (those with the longest path) are hosted into the thermal insulation of the internal channel.
- ❖ **Flanges:** various flanges are needed for different measuring and operative instrumentations. They are important since they create discontinuities (i.e. *thermal bridges*) in the upper thermal insulation of the tank; one will be worth of bigger attentions since it is opened towards the atmosphere.
- ❖ **Electrical heaters:** Two electrical heaters are installed in order to compensate the thermal losses and to avoid the freezing of the molten salts during no working periods; they are also used to reach the desired initial conditions of temperature inside the tank before the tests.
- ❖ **Structural supports:** they sustain the weight of the tank and keep it in position, lifted from the ground.

2.1.2 Materials

Table 2.1 List of the prototype materials

| MATERIAL | COMPONENTS |
|-----------------------------------|--|
| Hitec XL [®] | Molten salts |
| DelcoTerm [®] Solar E 15 | Diathermic oil |
| Rockwool | External thermal insulation: vertical and bottom part |
| Cerablanket [®] | External thermal insulation: upper part Internal channel thermal insulation |
| AISI 316 (austenitic steel) | Heat exchangers/oil rising tubes Impeller Internal channel Tank body Flanges |
| Carbon steel/Stainless steel | Structural supports |

The choice of some of these materials is worth to be argued. In particular, the DelcoTerm[®] Solar E 15 diathermic oil was chosen because it was the one already used in the existent plant in Benguerir. The choice of Hitec XL[®] as molten salts was instead due to the field operating conditions: the tank must operate below the maximum temperature of 300°C (limited by the linear Fresnel/oil system), and then *low temperature melting molten salts* were necessary. Hitec XL[®] is a *ternary mixture* of 15wt% of NaNO₃, 43wt% of KNO₃ and 42wt% of Ca(NO₃)₂ which, according to the material characterization carried out by the ENEA laboratories [1], has a freezing point that allows safe operation with the tank minimum temperature of 180°C.

2.1.3 Working Principle

The general working principle of a thermocline TES was presented in *section 1.3.2*, namely the thermal stratification within the tank due to density gradients. What characterizes instead this particular concept of thermocline TES is the integration of the heat exchangers connected by the internal channel, that allows the peculiar motion of the molten salts during both charge and discharge operation and should inherently enhance the thermal stratification.

During *charge transients* (schematically represented in **Figure 2.4**), hot oil enters the bottom heat exchanger from the top and progressively cools down, heating up the surrounding molten salts. As the salts heat up, their density reduces and they start moving upwards driven by buoyancy forces, so that the heat exchanger results in a countercurrent configuration. The quantity of hotter molten salts increases and starts to occupy the internal channel, now filled up with hotter salts than those in the rest of the tank: the resulting phenomenon is comparable to what happens in a chimney, with the so-called *chimney effect* pushing the hot salts, thanks to density difference, towards the top of the tank, where they stratify after having crossed the (inactive) discharge HX.

On the contrary, *discharge transients* (**Figure 2.4**) see the cold oil entering the top heat exchanger from the bottom and progressively heated up by the surrounding hot molten salts. This time, the salts cool down, their density increases and they are forced to move downwards by buoyancy forces, with, even in this case, a resulting countercurrent HX configuration. The chimney effect still takes place, similarly to the charge phase, but in the opposite direction, since the colder (heavier) molten salts are now inside the channel, and eventually stratify at the bottom of the tank after having crossed the (inactive) charge HX.

The role of the *impeller* should be those of helping or contrasting the buoyancy driving force, in order to obtain the desired flux inside the internal channel. Yet, as will be shown in *section 2.3*, its results have not been satisfactory.

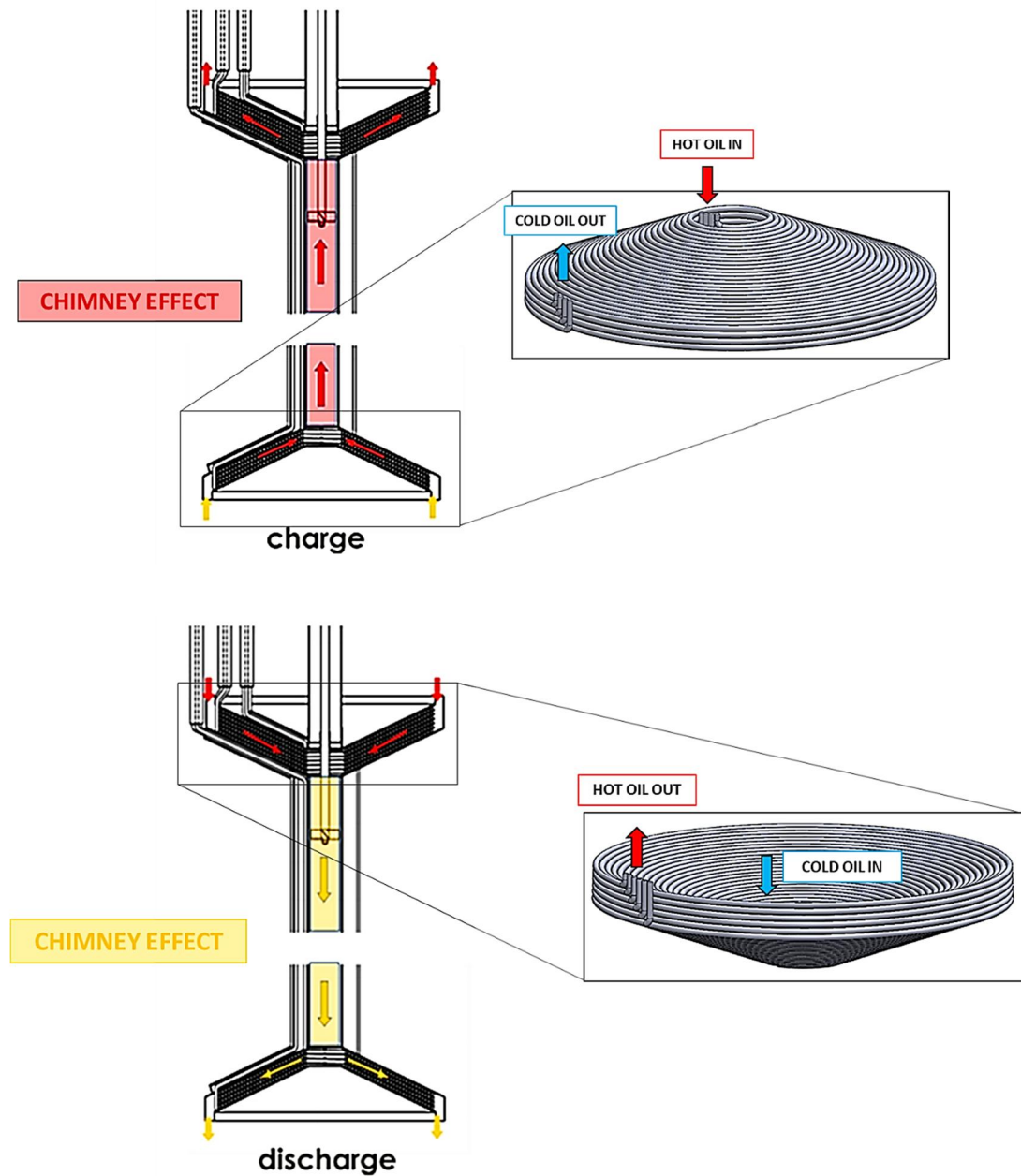


Figure 2.4 Schematic representation of the tank charge and discharge phases [23]

2.2 Description of the Testing Facility

2.2.1 Testing Circuit

The experimental loop is meant to reproduce the real operating conditions. Basically, two components other than the TES are important:

- ❖ the *electrical heater*, that warms up the oil going to the charge heat exchanger, simulating the solar field
- ❖ and the *air-cooler*, that cools down the oil coming from the discharge heat exchanger, replacing the underlying ORC cycle.

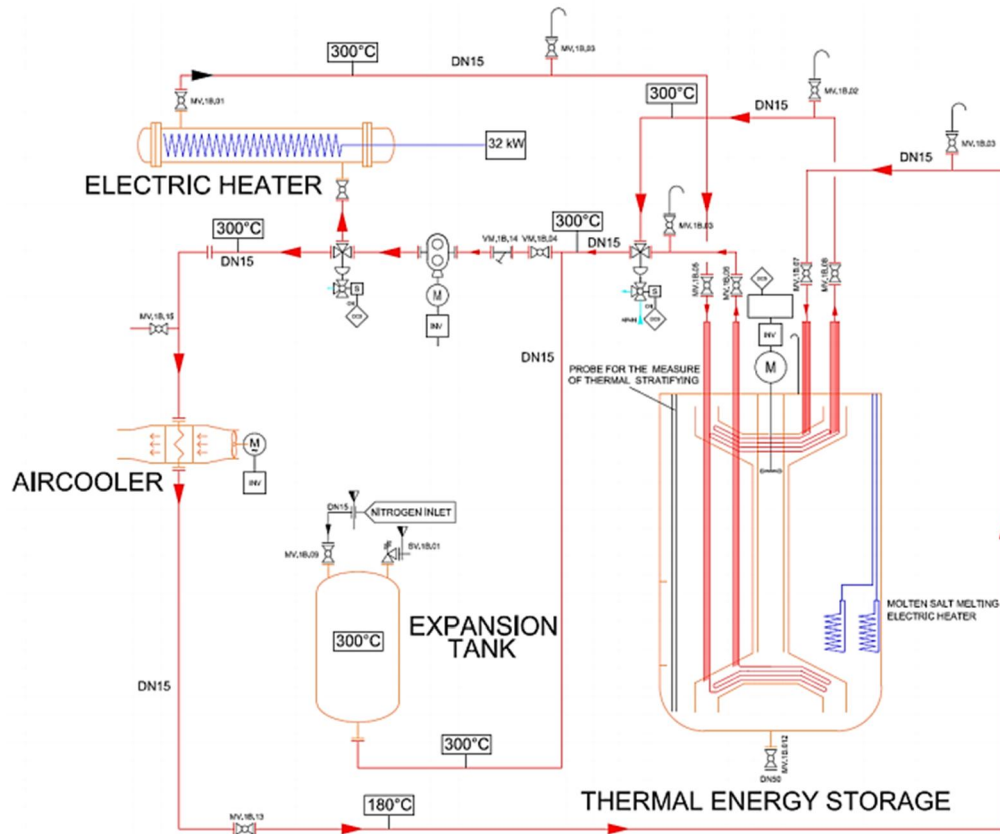


Figure 2.5 P&ID with the main components of the testing circuit [24]

2.2.2 Measuring Instrumentations

In order to have a useful diagnostic of the tests to analyse the experimental behaviour of the prototype, a series of measuring probes for the quantities of interest are installed in the testing circuit. The main instruments are shown in *Figure 2.6*, and commented here.

- ❖ **Temperature stratification:** it is measured by 12 thermocouples, placed 440 mm away from the axis of the tank. The thermocouples are equally spaced along the tank axis direction. The distance between two adjacent thermocouples is known, but the height of the first thermocouple from the tank bottom side was not recorded during the manufacturing process; it was assumed to be 101 mm. Therefore, a certain uncertainty exists about the absolute position of the thermocouples in the tank.
- ❖ **HX interface thermocouples:** for both the charge and discharge heat exchangers, two thermocouples are installed at the interface with the bulk molten salts, displaced one another of 180° along the azimuthal direction. They permit to measure the temperature of the molten salts at the inlet/outlet of the channel.
- ❖ **Oil side characterization:** the oil flow is completely characterized by a *mass flow-meter* on the circuit and by a thermocouple installed at both the inlet and the outlet sections of the charge and discharge heat exchangers.

Regarding instead the **molten salts mass flowrate** there is no instrumentation applied able to directly detect the mass flowrate of the molten salts inside the internal channel. However, this can be *indirectly estimated* through a simplified stationary power balance on the internal channel (while, in general, a transient phenomenon is actually taking place). As an example, for a charge transient:

$$\dot{m}_{MS,exp} = \frac{\dot{m}_{oil} \cdot \int_{T_{oil,out}}^{T_{oil,in}} c_{p,oil}(T) \cdot dT}{c_{p,MS} \cdot (T_{MS,out} - T_{MS,in})} \quad (2.1)$$

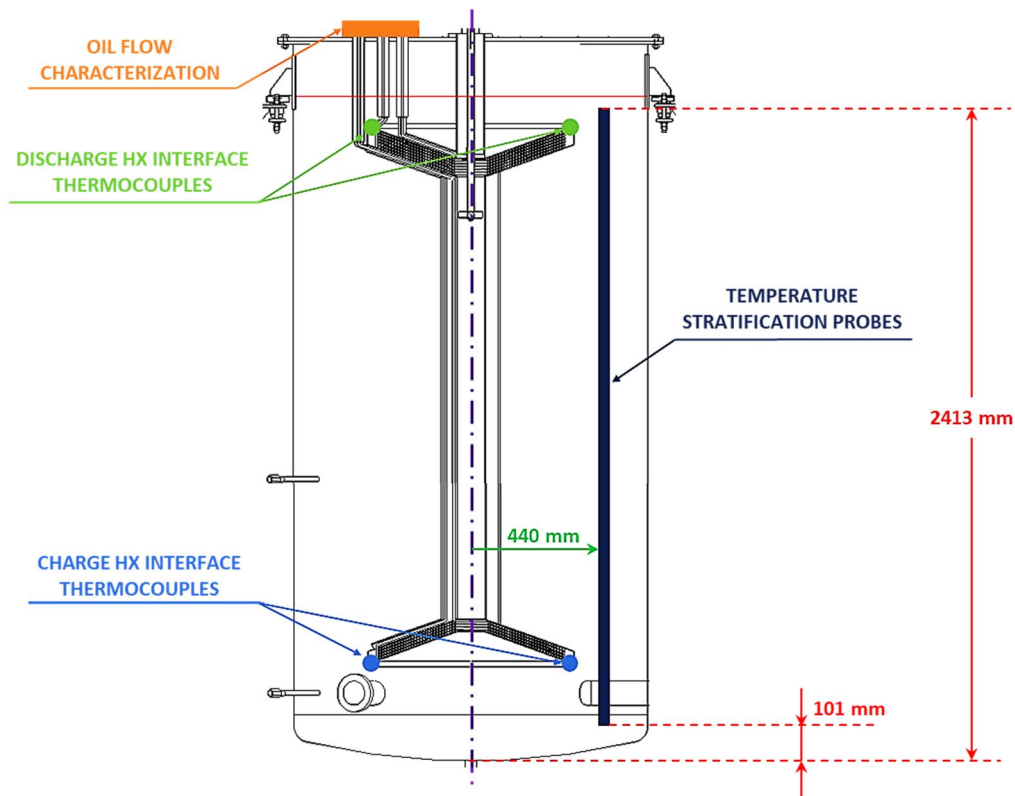


Figure 2.6 Scheme of the main measuring instrumentations installed

2.3 Experimental Data

The tests were carried out in the January of 2019 at the ENEA *Casaccia Research Center*. A data acquisition system able to collect the data from each installed sensor every 5 seconds was used. All the main possible operating conditions have been reproduced, performing in particular 7 discharge tests, 3 charge tests and 1 no-load test in order to assess the thermal losses.

Table 2.2 Outlook on the available tests

| TEST TYPE | Discharge | Charge | No-load |
|-----------|-----------|--------|---------|
| TESTS # | 7 | 3 | 1 |

The most explicative output of the tests is for sure the evolution of the temperatures at different heights of the tank, which allows at a glance to understand what was happening inside it during the transient.

2.3.1 Discharge Tests

Chronologically, they are the first that have been performed. The objective was, starting from selected tank charge conditions reached thanks to the integrated electrical heaters, to assess the capacity of the tank of heating up the oil above the temperature of 260°C (necessary for the underlying ORC cycle to work), and contextually to discharge completely until the minimum salts temperature of 180°C.

For the *discharge test 4* for instance, *Figure 2.7* and *Figure 2.8* show respectively the time evolution of the stratification temperatures and of the oil flow characteristics. The typical decreasing behaviour of the temperatures inside the tank can be noticed in the first 20 minutes, with the salts able to heat up the oil well above the target temperature of 260°C, but very far from reaching the minimum temperature of 180°C. However, around

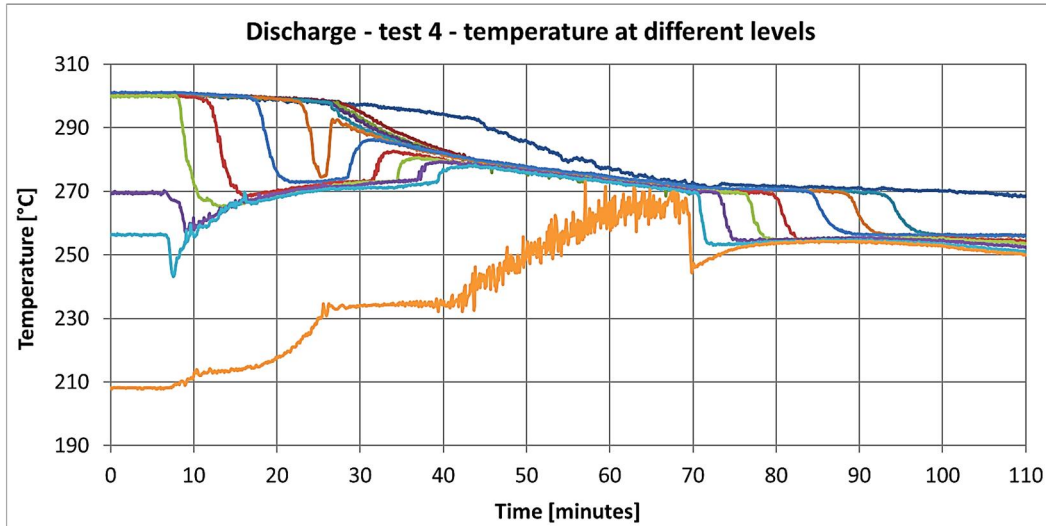


Figure 2.7 Tank temperatures evolution in discharge test 4

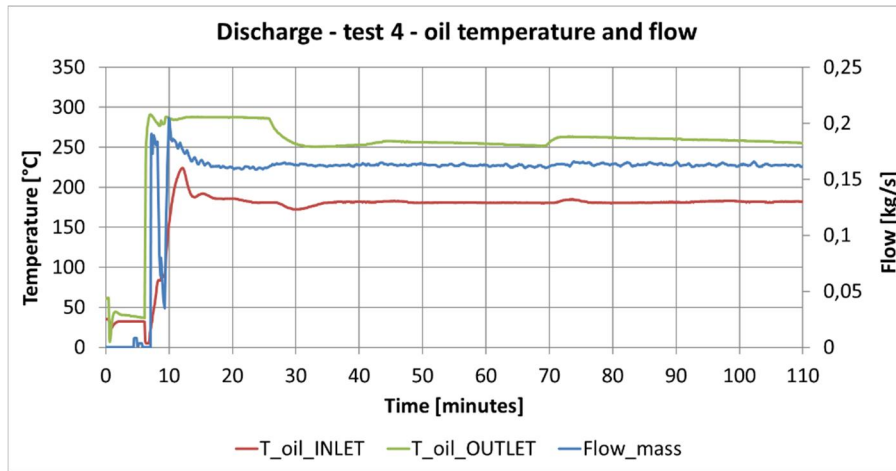


Figure 2.8 Oil flow characterization for discharge test 4

minute 25, the impeller was switched on in order to control the molten salts flux inside the internal channel, but the only result was the destruction of the previously set stratification, which is being restored starting only from minute 70 when the impeller was switched off. This explains the reason for which the impeller, after many tests, was not considered as a good regulation method. For this reason the last two discharge tests were carried out without using the impeller, resulting in a straightforward decreasing trend of all the thermocouples (see *Figure 2.9*).

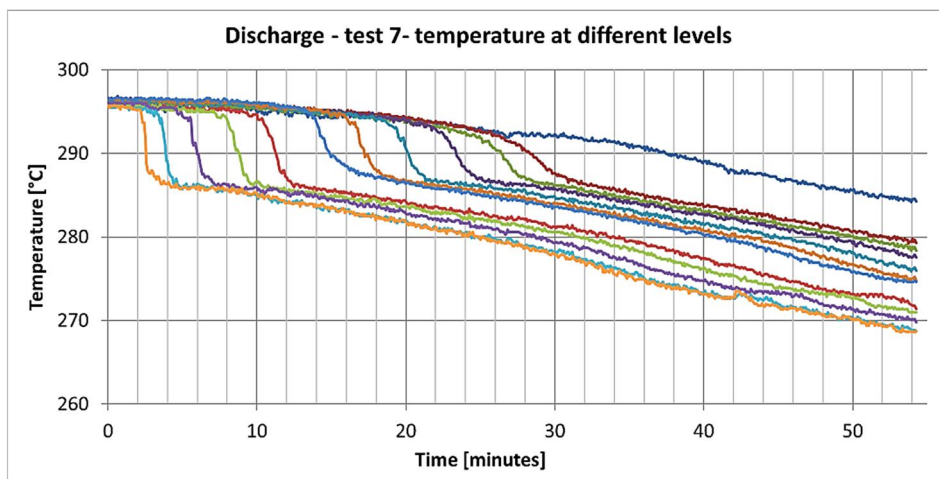


Figure 2.9 Tank temperatures evolution in discharge test 7

2.3.2 Charge Tests

Of the 3 tests available, one will be neglected since, due to a problem on the inlet oil thermocouple, there is no correct information about the heat load provided to the tank. During the useful *charge test 1*, as shown in *Figure 2.10* and *Figure 2.11*, despite an oil

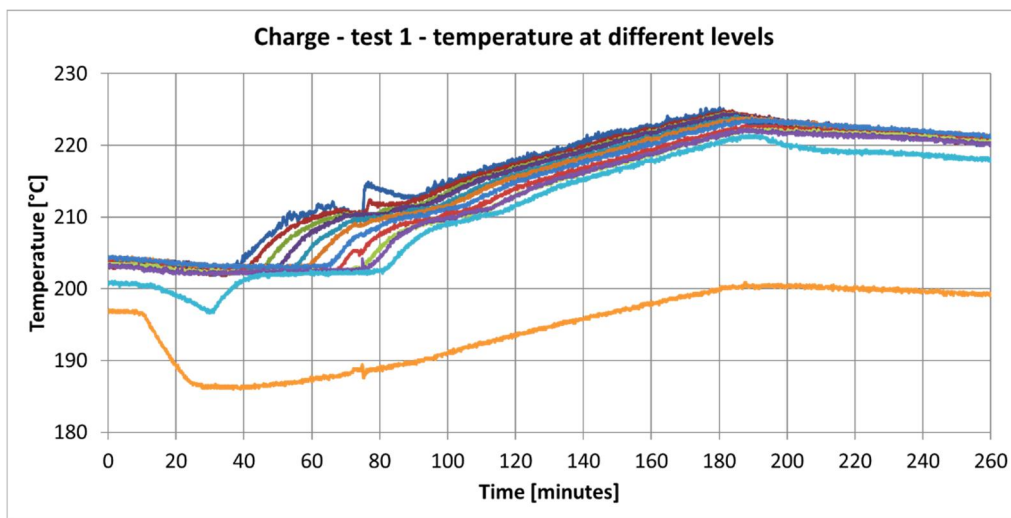


Figure 2.10 Tank temperatures evolution in charge test 1

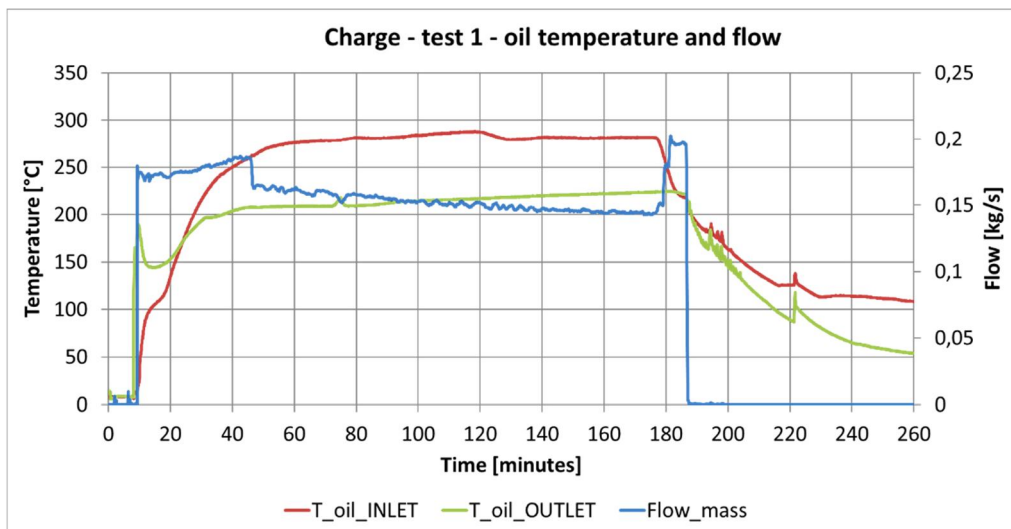


Figure 2.11 Oil flow characterization for charge test 1

inlet temperature very close to 300°C, the molten salts could reach very low maximum temperatures, probably due to the too high molten salts mass flowrate in the channel [24], and that is of course not a satisfactory charge result. Again, the impeller, besides not being able to reduce the molten salts flow, creates strong perturbations in the tank, as can be seen around minute 76. Then, the following test, the *charge test 2*, was performed without using the impeller. It does not present perturbations anymore, but still the desired maximum temperatures were far from being reached.

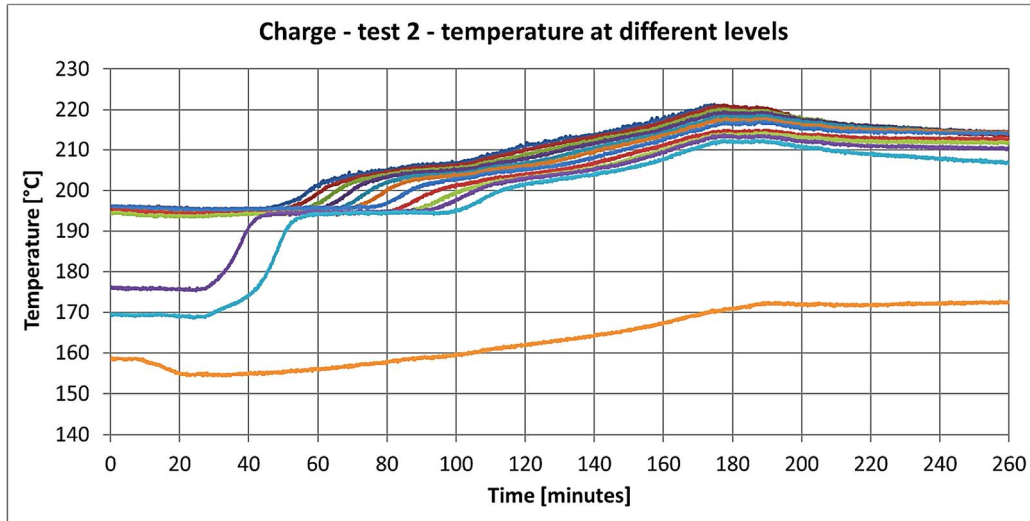


Figure 2.12 Tank temperatures evolution during charge test 2

2.3.3 No-Load Test

It is a test carried out without oil flowing into the tank, so no load is applied on the heat exchangers. The objective of this test was to evaluate the capacity of the tank of maintaining the charge condition during time, assessing the thermal losses towards the environment. The tank was then left inactive for almost 18 hours, starting from an initial condition of uniform temperature at around 263°C, set thanks to the integrated electrical heaters. The parameter that most clearly attests this phenomenon is the decreasing *average temperature* inside the tank (*Figure 2.13*), simply computed as the arithmetic average of the values provided by the 12 stratification thermocouples.

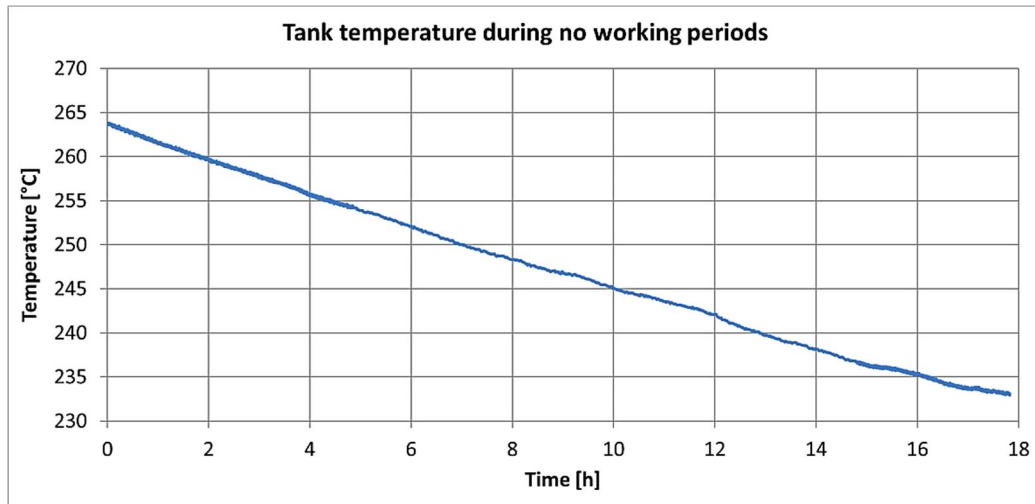


Figure 2.13 Evolution of the average tank temperature during a no-load transient

Chapter 3

3. Development of the CFD Model

Computational Fluid Dynamics (CFD) is a very powerful technique that enables to accurately reproduce and analyse fluid flows and heat transfer phenomena, by solving numerically the partial differential (or integro-differential) equations of mass, momentum and energy conservation, transformed into a system of algebraic equations through suitable temporal and spatial discretization methods [25]. This is achieved by using the commercial CFD software named *STAR-CCM+* [26], in which spatial discretization is performed with the *Finite Volumes Method* by subdividing the domain into a finite number of smaller *Control Volumes* (CVs), onto which the integral conservation equations are applied and appositely approximated [27]. The objective of this work is to develop a CFD model able to reproduce the transient behaviour of the thermocline prototype with a reasonable computational cost.

3.1 Choice of the Model Dimensionality

The computational cost increases as the number of CVs increases, and then as the number of algebraic equations to be solved increases. A good solution for reducing the computational cost (that otherwise, especially for transient simulations, would be very high) is to exploit possible symmetries, in order to reduce the domain to a smaller section representative, in this case, of the whole tank. In particular, a consolidated solution in literature, even when dealing with thermocline TES with integrated heat exchangers, is

the use of a *2D axisymmetric domain*, which ensures an acceptable accuracy while keeping a reasonable computational cost [16, 28]. Anyway, to have the possibility of applying this procedure, both the *thermal load* and the *physical domain* need to be axisymmetric.

- ❖ As per what regards the *thermal load*, two contributions should be considered, namely the thermal losses towards the environment and the charge or discharge load. The thermal losses are axisymmetric once it is assumed that the convective heat transfer coefficient is uniform in the azimuthal direction. The charge (or discharge) load is applied through heat exchangers having a conical coil shape with 28 loops and a very small pitch of around 3.7 mm, in which the oil experiences in typical conditions a total temperature difference of about 100°C, and then presenting acceptably small temperature variations on each loop in the azimuthal direction. As a proof, the measurements of the symmetric interfaces thermocouples presented in *Figure 2.6* can be compared, showing a temperature difference well below 5°C for most of the time, apart from a peak around minute 30 of the discharge test 4, corresponding to the impeller perturbations (*Figure 3.1* and *Figure 3.2*).

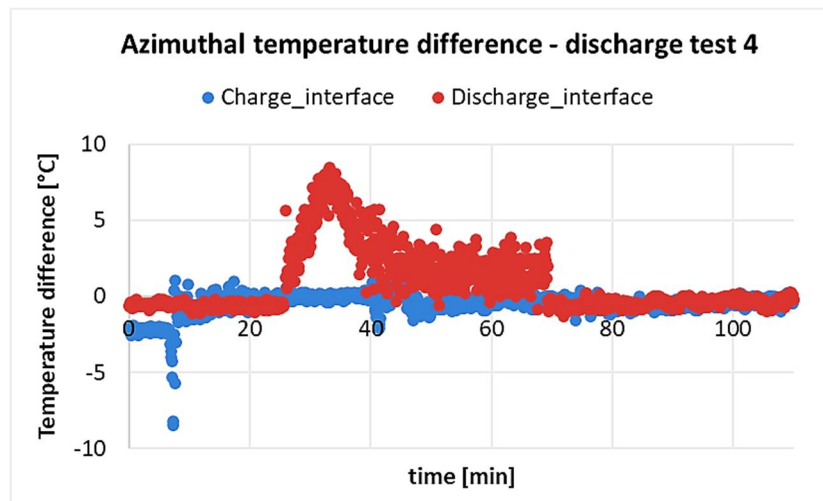


Figure 3.1 Azimuthal temperature difference from the interfaces thermocouples during discharge test 4

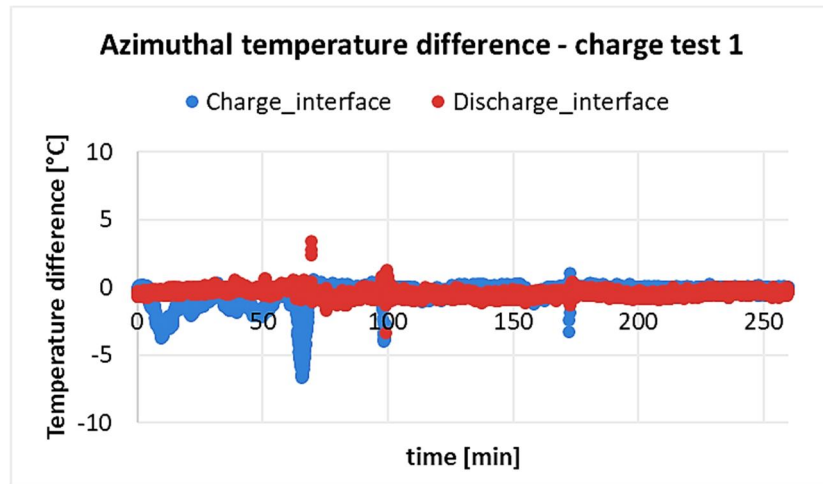


Figure 3.2 Azimuthal temperature difference from the interfaces thermocouples during charge test 1

- ❖ Regarding instead the *physical domain*, the prototype is basically a cylindrical tank, containing a tubular channel on its axis and two heat exchangers that, as just discussed, can be approximated as axisymmetric. The main components of the tank are then axisymmetric, but *few minor simplifications* of the other accessory components must be performed in order to obtain a *fully axisymmetric 2D geometrical domain*. They are listed in the next section, while presenting the computational domain.

3.2 Definition of the Computational Domain

All the hypothesis made in order to obtain a fully axisymmetric domain representative of the real prototype are now presented and justified. At the end, the characteristics of the computational domain in terms of boundaries and included regions will be discussed.

3.2.1 Simplification of the Minor Components

Those components that occupy a small volume with respect to the whole tank, or a small azimuthal angle, or that in any case are not important for the active operation of the prototype during the tests, have been simplified for symmetry purposes. Starting in fact from the complete and detailed tank presented in **Figure 2.1**, the modifications listed in

the table below have been applied to the real geometry in order to obtain a fully axisymmetric domain representative of the real situation (appreciable in *Figure 3.3*).

Table 3.1 Summary of the geometry simplifications

| COMPONENT | ACTION | CONSEQUENCE |
|---|---|---|
| Oil rising tubes | Not included in the domain | Calibration of the thermal conductivity of the insulant on the tank top |
| Electrical heaters | Not included in the domain | Calibration of the thermal conductivity of the insulant on the tank side |
| Structural supports | Not included in the domain | Calibration of the thermal conductivity of the insulation on the tank side |
| Flanges (excluded the one opened towards the atmosphere) | Not included in the domain | Calibration of the thermal conductivity of the insulant on the tank top |
| Flange opened towards the atmosphere | <ul style="list-style-type: none"> ○ Shifted on the tank axis for symmetry purposes ○ Represented as an aperture with air facing the atmosphere | Elimination of the impeller shaft and its tubular casing <i>above</i> the salts level |

An *equivalent thermal conductivity* on the external insulations is introduced to take into account the effects of the thermal bridges caused by the neglected components. This equivalent thermal conductivity requires a dedicated calibration; see *section 3.6*. Regarding the open flange (last item of the table), the methodology adopted, i.e. moving the component on the tank axis, is based on the literature [16, 28]. In these works, the steam generator, integrated inside the storage, was shifted on the tank axis for symmetry purposes with satisfactory final results. The shift of the open flange requires removing

the impeller shaft and its casing in order to create a path for the hot air to leave the top of the tank toward the atmosphere (as highlighted in *Figure 3.3*)

3.2.2 Impeller

Given the unsatisfactory behaviour of the impeller during the experimental campaign, it was decided to consider the impeller as a passive element only, and then to develop and validate the model just against those transients in which the impeller was switched off.

Furthermore, after fluid dynamics evaluations (*Appendix A*), the best option for a bi-dimensional axisymmetric reproduction of its effect on the salts flux was considered those of including in the computational domain only the shaft, without the profile of the blades.

3.2.3 Resulting Computational Domain

The 2D fully axisymmetric computational domain obtained through the aforementioned considerations, is a *half section* of the tank, shown in *Figure 3.3* with some highlights on its main characteristics. The computational domain contains of course the molten salts, the air region above them in connection with the atmosphere, the structure of the internal channel, the inactive impeller, the tank body, the internal channel thermal insulation, and finally uniform external thermal insulation layers on the top, on the side and on the bottom of the tank. The CFD model will compute the conjugate heat transfer at the interface between regions with different materials. The reader can refer to *Table 2.1* for the list of the particular materials each region consists of, and to *Appendix B* for the thermophysical properties of these materials.

Also, it is very important to notice that, in correspondence with the integrated heat exchangers, the computational domain ends on the external wall of the tubes, and so that

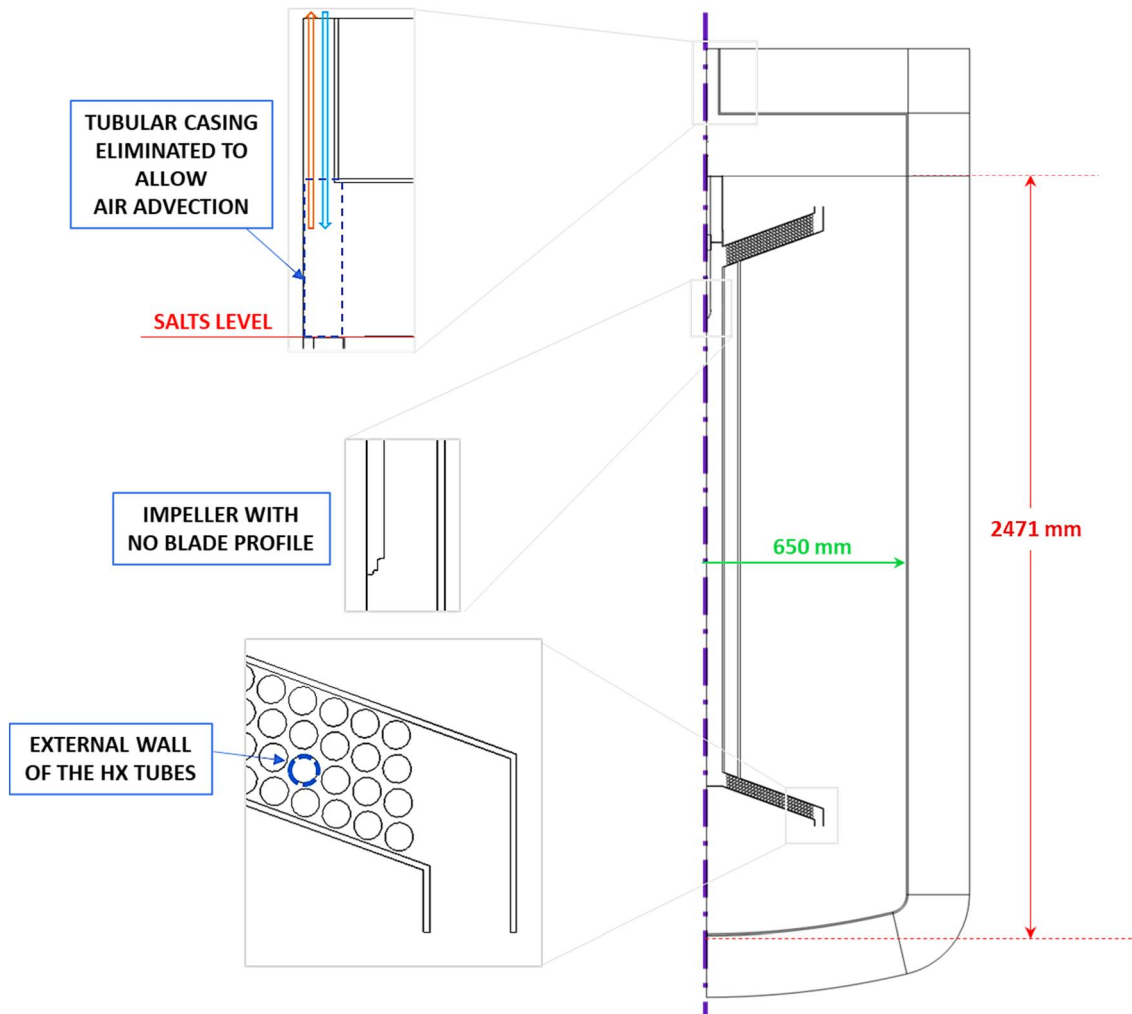


Figure 3.3 Computational domain representation and highlights on the main features

it does not contain the tube walls and the diathermic oil flowing inside them. This choice allows a strong reduction in the number of cells and allows to exempt the model from solving also the oil flow. However, both the conductive and convective contributions in the application of the heat load, will be considered in a suitable *Boundary Condition (BC)*.

3.3 Boundary Conditions

Boundary Conditions (BCs) are one of the main features in the definition of a CFD model. They are the expression of whatever happens outside the computational domain but still has an influence on its behaviour. In the case under exam, specific BCs will be used for applying the heat load to the storage through the heat exchangers, and for defining the heat losses towards the atmosphere. Also, since transient conditions will be simulated by the model, proper Initial Conditions (ICs) need to be defined too.

3.3.1 Heat Exchangers: Heat Load

In the heat exchangers, 3 contributions to the heat transfer can be distinguished:

- ❖ convection on the molten salts side (shell side);
- ❖ conduction in the radial direction in the tube wall;
- ❖ convection on the oil side (tubes side).

Provided that, as previously stated, the computational domain contains the MS, but not the tube wall and the oil, the corresponding BC must take into account the last two items, while the first one will be intrinsically computed in the CFD simulation.

The driving phenomenon here is the convection on the oil side, so a *Robin Boundary Condition* is necessary, meaning that a *heat transfer coefficient* (HTC) and a *temperature* must be provided at each boundary. Reminding that the heat exchangers are composed

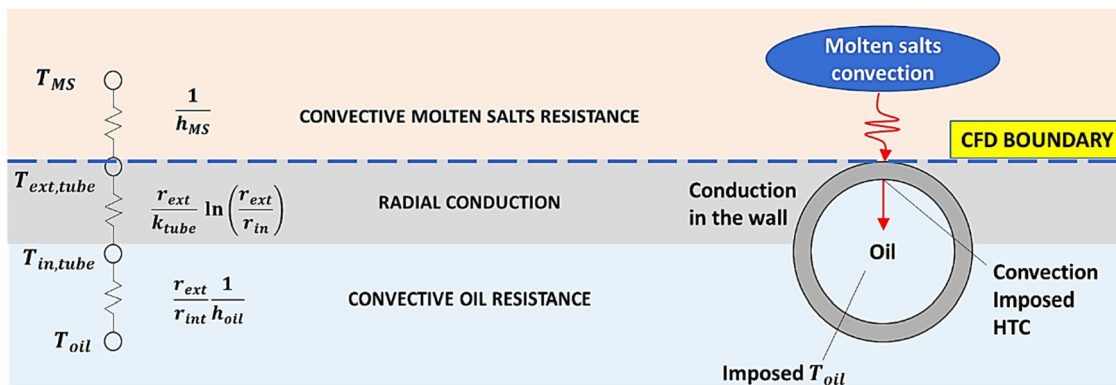


Figure 3.4 Schematic representation and electrical equivalent of the heat transfer in the heat exchangers

by 4 (charge) or 6 (discharge) serpentine crossed in parallel by an oil flux of which are known, every 5 seconds, the total mass flowrate and the inlet and outlet temperatures (see sections 2.2 and 2.3), the following hypothesis are made:

- ❖ each serpentine shares the same quantity of the total mass flowrate;
- ❖ as a first approximation, the heat flux on the tube walls is considered as uniform.

Another important aspect to be highlighted is that this boundary condition will be *variable in time*, according to the experimental data collected during the tests.

3.3.1.1 Oil Temperature

Provided the hypothesis of uniform heat flux, from the theory it is known that the mean temperature inside the tubes will have a linear variation along the axial direction [29]. A MATLAB[®] script have then been developed able to compute the mean temperature of each loop of the serpentine under the hypothesis of linear variation of the temperature with the coil length, starting from the inlet and outlet temperatures ($T_{oil,in}$ and $T_{oil,out}$) experimentally measured at each timestep. As an example, for the charge HX, if the i^{th} loop starts at the section $K = i$ and ends at the section $K + 1$, then its mean temperature is given by the equations:

$$\begin{aligned} \bar{T}_{oil,loop,i} &= \frac{T_{oil,section,i} + T_{oil,section,i+1}}{2} \\ T_{oil,section,K} &= T_{oil,in} - \sum_{j=1}^{K-1} \frac{L_{loop,j}}{L_{tot}} (T_{oil,in} - T_{oil,out}) \end{aligned} \quad (3.1)$$

The results are produced in a tabular form compatible with the integration in the CFD software STAR-CCM+, obtaining the typical condition shown in *Figure 3.5*.

3.3.1.2 Heat Transfer Coefficient

The contributions of the oil convection and of the radial conduction in the tube wall must be taken into account by this parameter:

$$U_{oil+tube} = \left[\frac{r_{ext}}{k_{tube}} \ln \left(\frac{r_{ext}}{r_{in}} \right) + \frac{r_{ext}}{r_{in}} \frac{1}{h_{oil}} \right]^{-1} \left[\frac{W}{m^2 K} \right] \quad (3.2)$$

But, if the first term depends only on geometrical parameters and on the thermal conductivity of the tube material and then it is constant and uniform, the second depends on the oil *convective heat transfer coefficient* h_{oil} , which must be evaluated through a dedicated correlation. A correlation for conical coil heat exchangers with aperture angle of 135° (very close to the 140° of the heat exchangers of the prototype) was found in literature [30] and its suitability for the case under exam verified against reference operational conditions data. The correlation is:

$$\bar{h}_{oil} = \frac{k_{oil}}{d_{tube}} \cdot 0.136 \cdot De_{oil}^{0.8} \cdot Pr_{oil}^{-0.190} \quad (3.3)$$

where Pr_{oil} is the oil *Prandtl Number* and the De_{oil} is the *Dean Number*, a typical non-dimensional parameter for curved internal flows, that introduces on the HTC the influence of secondary flows due to the curvature of the tube:

$$De_{oil,i} = Re_{oil,i} \sqrt{\frac{r_{in}}{R_{loop,i}}} \quad (3.4)$$

with Re_{oil} the *Reynolds Number*, r_{in} the *inner diameter of the HX tube* and R_{loop} is the *curvature radius* relative to the loop. Since the coil is conical, the curvature radius varies with each i^{th} loop, and then the Dean number, h_{oil} and consequently also $U_{oil+tube}$ will be different for each wall boundary, according to the curvature radius. Again, a

MATLAB[®] script able to compute $U_{oil+tube,i}$ for each position, at each timestep, was produced.

3.3.2 Convective Thermal Losses

A *Robin BC* is imposed on the external surface of the tank in order to account for the convective heat losses with the atmosphere. Therefore, the ambient temperature and the HTC (both uniform and constant) have to be imposed.

- ❖ For what regards the temperature, the average temperature in Rome for each test day was retrieved from an online meteorological archive [31].
- ❖ For the calculation of the heat transfer coefficient instead, it is considered as a function of the wind velocity only and calculated by means of suitable correlations. Since no data was available, the wind velocity was arbitrarily set as $v_{wind} = 7 \text{ m/s}$. In particular, for the vertical external walls, the *Churchill and Bernstein* correlation [29] for a cylinder in cross flow was selected:

$$\bar{h}_{vert} = \frac{k_{air}}{D_{tank}} \left\{ 0.3 + \frac{0.62 Re_D^{\frac{1}{2}} Pr^{\frac{1}{3}}}{\left[1 + (0.4/Pr)^{\frac{2}{3}} \right]^{\frac{1}{4}}} \left[1 + \left(\frac{Re_D}{282000} \right)^{\frac{5}{8}} \right]^{\frac{4}{5}} \right\} \quad (3.5)$$

$$Re_D Pr \gtrsim 0.2$$

$$D_{tank} = 1.7 \text{ m}$$

A correlation for mixed flow over flat plates was applied instead on the top horizontal wall and on the bottom part (approximatively flat) [29]:

$$\bar{h}_{hor} = \frac{k_{air}}{L_{tank}} (0.037 Re_L^{4/5} - 871) Pr^{1/3}$$

$$0.6 \lesssim Pr \lesssim 60$$

$$5 \times 10^5 \lesssim Re_L \lesssim 10^8$$

$$L_{tank} = D_{tank} = 1.7 \text{ m}$$
(3.6)

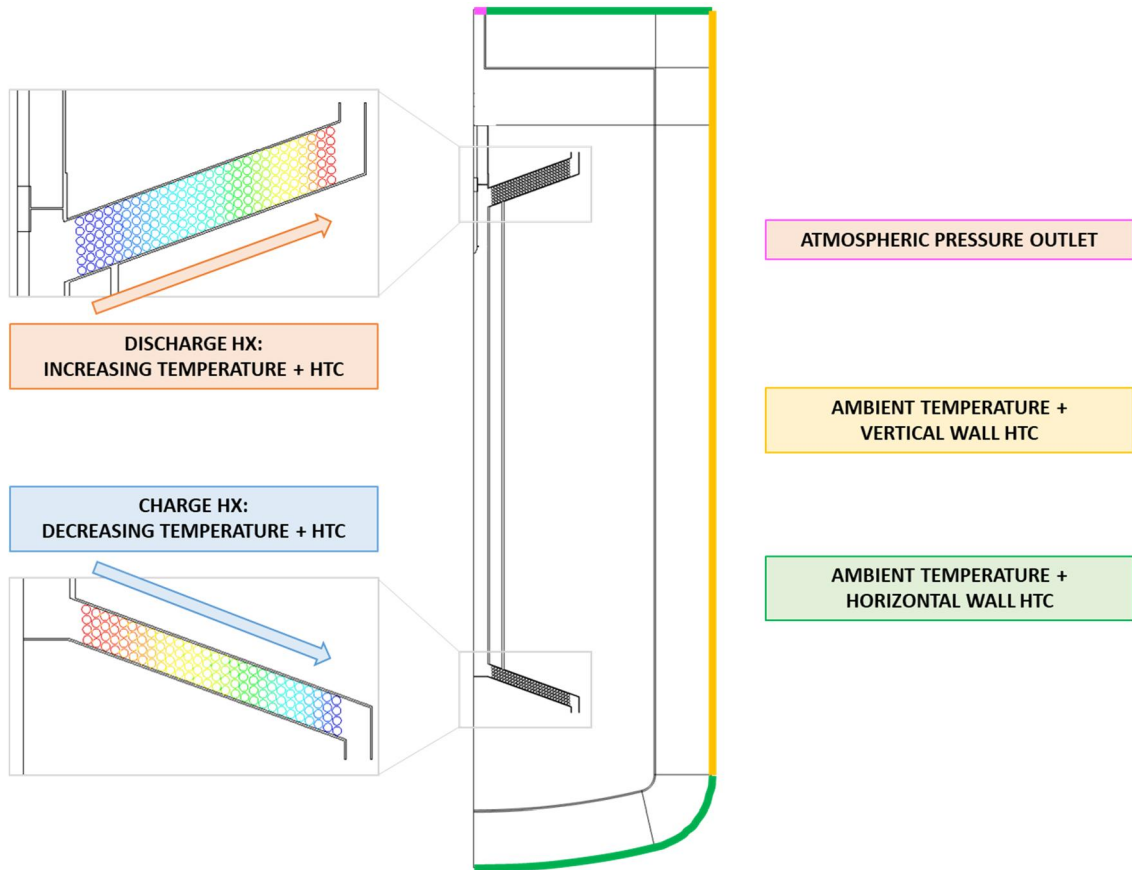


Figure 3.5 Resuming scheme of the Boundary Conditions

3.3.3 Advective Thermal Losses

They are due to the exchange of air with the environment. Simply, corresponding with the aperture, a *pressure outlet* with ambient temperature and ambient pressure is set. A scheme for resuming all the BCs applied and to highlight their positions is reported in *Figure 3.5*.

3.3.4 Initial Conditions

Initial conditions are necessary in order to set the tank configuration from which the simulation starts. In some cases the simulations will reproduce just a fraction of the experimental test (e.g. after that the impeller has been switched off), and then both a temperature and a velocity initial condition must be provided, starting from the data at the selected timestep, in order to reproduce a transient already occurring.

Table 3.2 List of the Initial Conditions applied

| INITIAL CONDITION | POSITION | SOURCE |
|----------------------------|---|---|
| Temperature stratification | Bulk Molten Salts Internal solid regions | 12 axial stratification thermocouples |
| Channel temperature | Internal Channel (MS) | Interface thermocouples corresponding to the inactive HX |
| Solid temperatures | External insulation layers Tank body | Iterative from CFD (starting from tentative condition) |
| Molten Salts velocity | Internal Channel (MS) | Experimental estimation of the molten salts mass flowrate (2.1) |

Regarding the internal channel, a uniform temperature and velocity IC is imposed starting from the only data available, while the temperature IC on the external insulation layers is iteratively improved starting from a tentative temperature distribution, in order to be able

to account for the right amount of thermal losses from the very beginning of the simulation.

3.4 Main Features of the Model

- ❖ **Axisymmetric:** all the gradients and velocity components in the direction perpendicular to the computational domain are null.
- ❖ **Gravity:** the contribution of gravity is included in the model in order to reproduce the buoyancy forces inside the molten salts, crucial for the correct simulation of the tank behaviour.
- ❖ **Implicit time scheme:** it was chosen due to its robustness and its unconditional stability for whichever timestep size [27].
- ❖ **Conjugate heat transfer:** the model is able to compute the heat transfer at the interface between different media.
- ❖ **Turbulence model:** it is necessary in order to simulate the mixing that occurs within the molten salts, especially where the salts are poured into the tank from the internal channel interfaces. The *Menter SST* $\kappa - \omega$ two equations turbulence model was selected due to its capability of effectively dealing with both near-wall and fully turbulent regions [27]. Furthermore, it was already demonstrated to provide good results in similar simulations [16].
- ❖ **All y^+ wall treatment:** the *non-dimensional wall distance* y^+ , which is in practice a Reynolds number in which the *distance from the wall* y is the characteristic dimension of the phenomenon, must be introduced. One possible interpretation of the Reynolds number is to see it as the ratio between *inertia forces* and *viscous forces*. It can be noticed then, that as y goes to zero (i.e. as the wall is approached), the y^+ will reach the value 1 or will even become smaller: at this point, viscous forces will have become of the same magnitude, or even more important, than the inertia forces. As a consequence, even a turbulent flow (generally inertia-dominated), becomes laminar in a certain region next to the wall, named *viscous sub-layer*, characterized by values

of $y^+ \sim 1$. This region has an important macroscopic effect for example in the evaluation of pressure drops. In CFD, the capability of a turbulent model to reproduce the physics of this region strictly depends on the y^+ defined by the position of the centre of the first cell adjacent to the wall (better if $\lesssim 1$) and on the characteristics of the model itself.

Provided that, as will be shown in the next *section 3.5*, the mesh will not reach the highest degree of definition (i.e. with the application of *prism layers*) on all the walls, the *all y^+ wall treatment* has been chosen since it allows a satisfactory resolution of the flows in whatever y^+ condition, and then both on refined and not refined walls.

With the application of these models, all the characteristic phenomena that define the behaviour of a thermocline TES, alongside with those that are responsible of its loss of efficiency (all presented in *section 1.3.2*), will be accounted for in the simulation.

3.5 Definition of the Computational Mesh

Computational Fluid Dynamics is a numerical approach, and then requires the *discretization* of both the *spatial domain* and *temporal domain*. If on one side the temporal discretization simply requires the subdivision of the time interval of the simulation into smaller *timesteps*, on the other side the spatial discretization (the so-called *meshing*) requires a more curtailed design, in order to find a trade-off between the accuracy and the computational cost of the simulations.

3.5.1 Characteristics of the Mesh

A *polygonal mesh* has been applied on the computational domain, which ensures a balanced and efficient solution also for complex geometries. The mesh has been refined the most in the fluid regions (blue ones in *Figure 3.6*), where all the conservation equations must be solved, and has been left coarser in solid regions (white ones in *Figure 3.6*), where only the energy equation must be solved. *Prism layers* have been applied onto walls where the very accurate solution of temperature and velocity gradients was

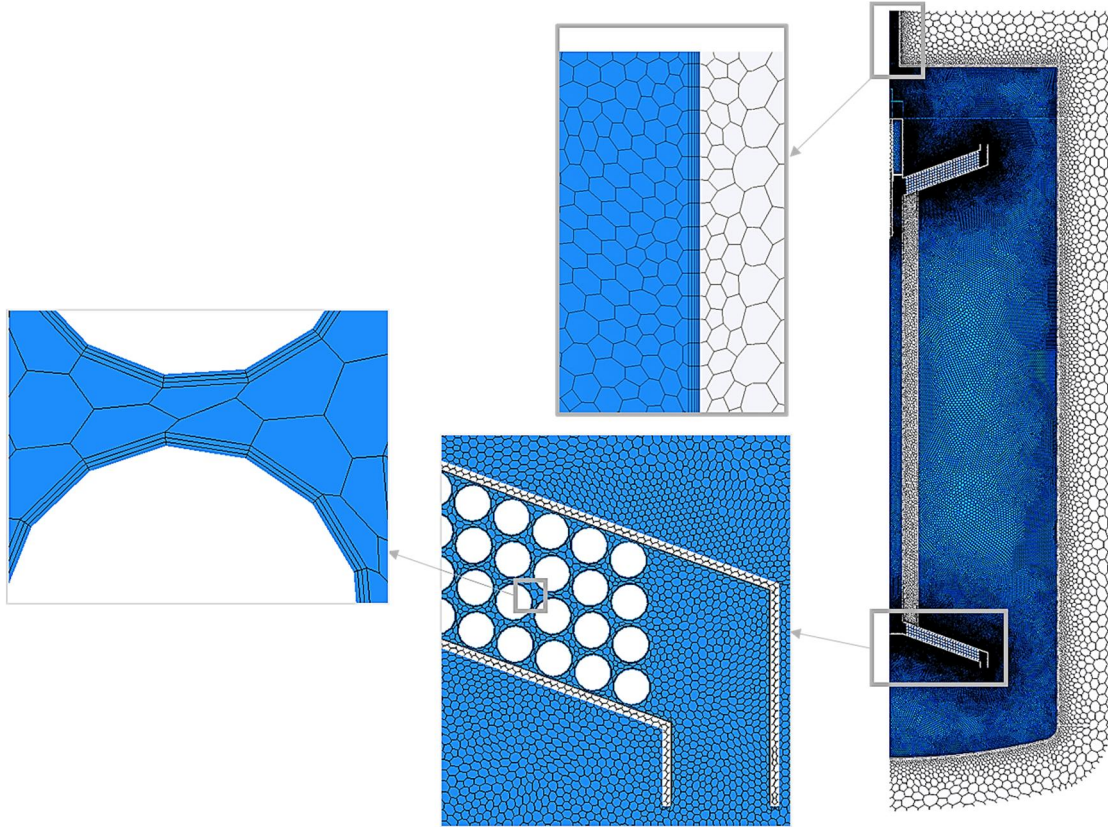


Figure 3.6 Mesh and details on prism layers

necessary, like in the atmospheric aperture channel and most of all on the HX walls, where the heat load and the pressure drop resulting from a very congested region must be accurately assessed. Here 3 prism layers with a total thickness of 0.35 mm were applied, that ensure a value of $y^+ \lesssim 1$.

3.5.2 Mesh Independence Study

A template operative charge transient of 3600 s, starting from a uniform stratification temperature of 202°C and with constant oil inlet and outlet temperatures ($T_{oil,in} = 271^\circ\text{C}$

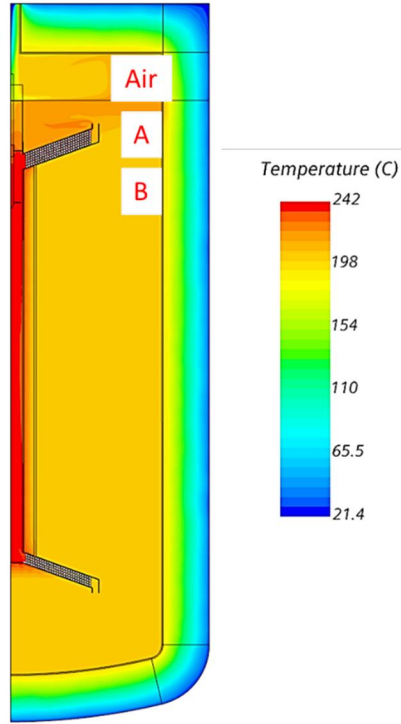


Figure 3.7 Result at the end of the transient and positions of the fictitious probes

and $T_{oil,out} = 208^{\circ}\text{C}$) retrieved from a selected timestep of the *charge test 1*, was simulated with a *timestep* of 15 s, using meshes with different number of cells obtained varying the cell base size. Three fictitious temperature probes (Air, A, B, see *Figure 3.7*) were placed for measuring parameters differently influenced by the transient modifications, and also the average temperature of the molten salts was measured. The results are resumed in the plots in *Figure 3.8*. *Temperature A* is the one that experiences the biggest variations during the charge transient, so its plot is the one that better shows the convergence with respect to the most refined solution, that is very good already for a number of 1.08×10^5 cells, corresponding to a base size of 4 cm and indicated with a red spot.

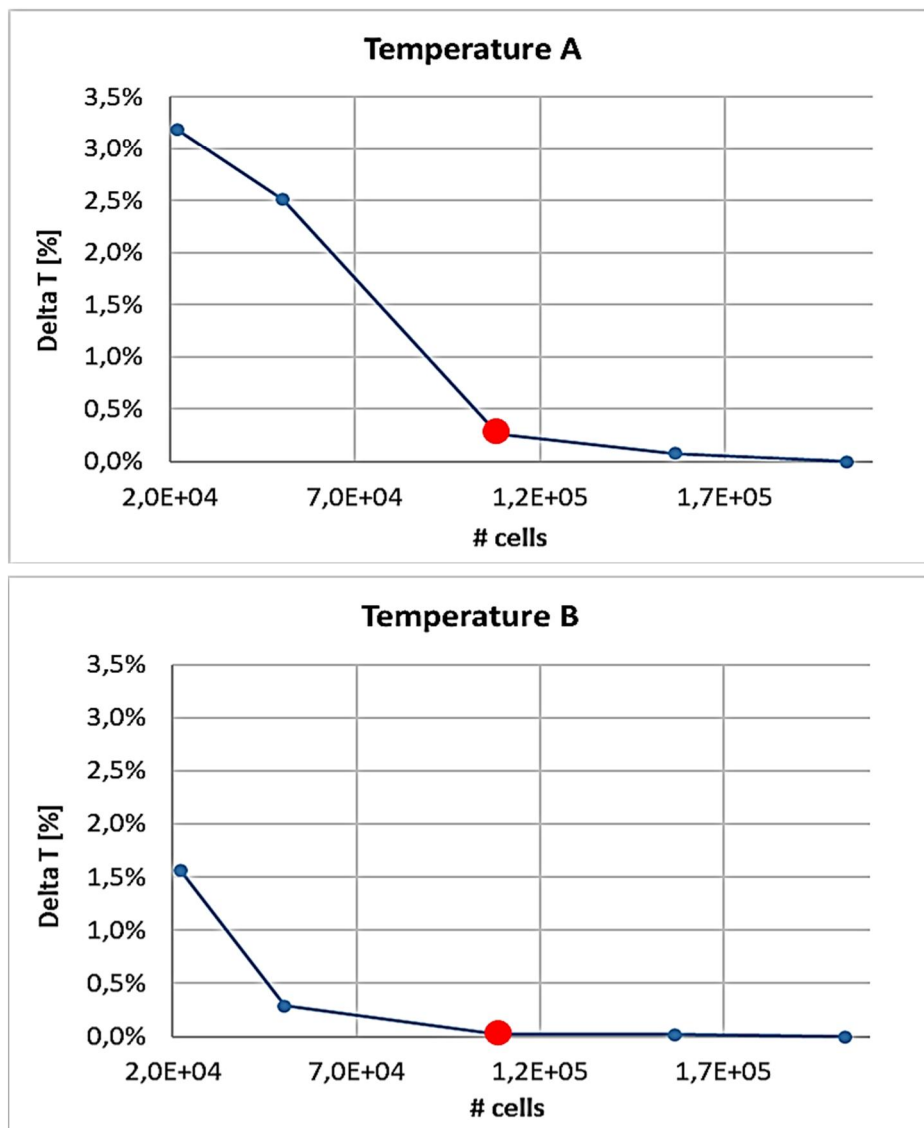


Figure 3.8 Sample outcomes of the mesh independence study

3.5.3 Timestep Independence Study

The simulation of the same template charge transient has been carried out also varying the length of the timestep, showing the convergence behaviour shown in *Figure 3.9*. Here a **2.5 s timestep** was selected as a trade-off between accuracy and time-consumption: a 3% error with respect to the solution with timestep of 1 s was considered acceptable in order to reduce the simulation time of almost 3 times.

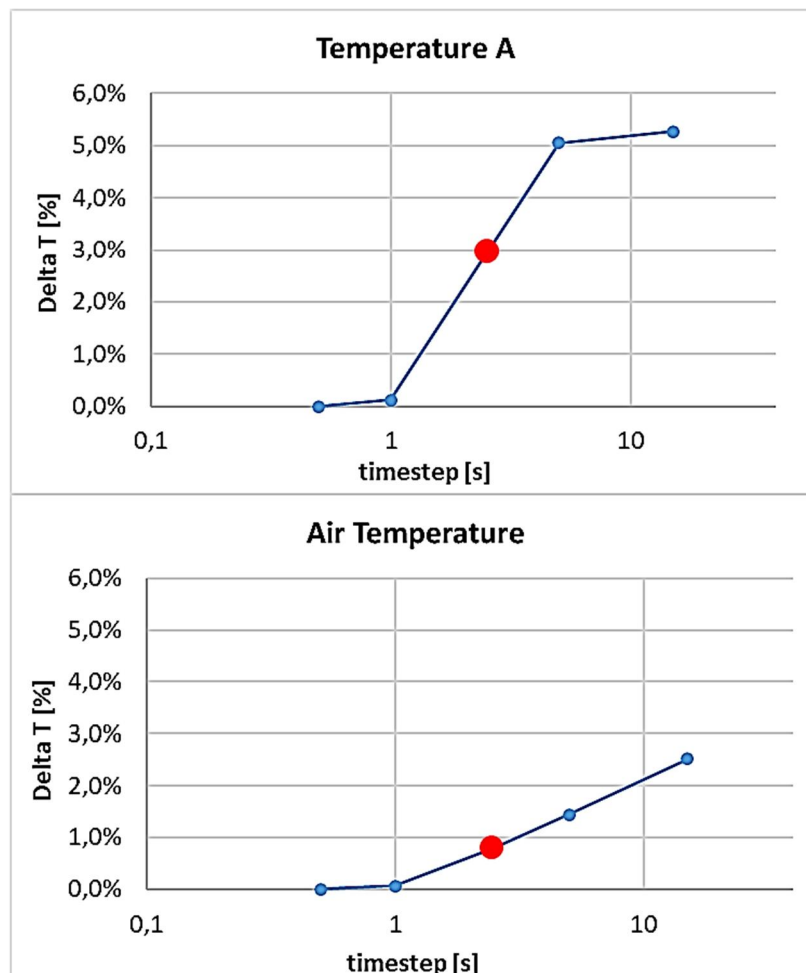


Figure 3.9 Outcomes of the timestep independence study

| SELECTED COMPUTATIONAL MESH | |
|-----------------------------|--------------------|
| # cells | 1.08×10^5 |
| Timestep | 2.5 s |
| Computational Time | ~ 38 minutes |

3.6 Calibration of the Thermal Losses

As anticipated in *section 3.2.1*, the geometrical simplifications introduced to obtain an axisymmetric domain lead to an underestimation of the thermal bridges, that has to be compensated by calibrating the thermal conductivity of the insulation layers. For this purpose, the *no-load test* presented in *section 2.3.3* is used. It is characterized by an initial stratification temperature almost uniform at around 263°C, and the ambient temperature is considered of 7°C.

Firstly, it has been simulated with the original model presented above, namely with the uniform layers of thermal insulation characterized by their actual thermal conductivities, using as representative parameter, as previously suggested, the *average temperature* of the molten salts. The plot in *Figure 3.10* shows that, in this way, the evolution of the average MS temperature is completely different from the experimental one, demonstrating the presence of a high underestimation of the thermal losses.

Then, the model has to be *calibrated*, setting an *equivalent thermal conductivity* to the insulation layers, able to reproduce the same global effect as the one that the neglected thermal bridges would have caused. A rough calculation, considering in a power balance the relative surfaces of insulant and steel components together with their actual thermal conductivities, gave a hint about the values of equivalent thermal conductivity from which to start the calibration in the different parts of the tank. Eventually, an optimal configuration was found, assigning the values shown in *Table 3.3*, giving the very good result shown in *Figure 3.11*, with thermal losses that, with this configurations, have a value of roughly 4 kW.

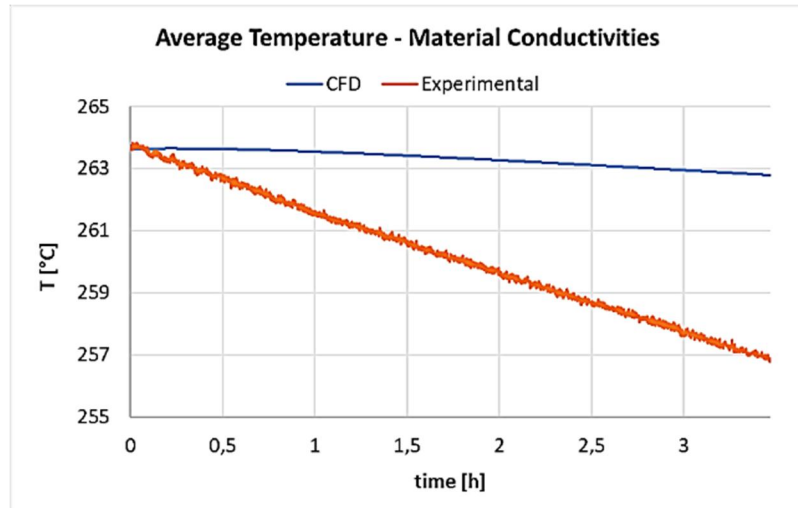


Figure 3.10 Average MS temperature evolution comparison using actual insulant conductivities

Table 3.3 Equivalent thermal conductivities applied

| REGION | ORIGINAL CONDUCTIVITY $\left[\frac{W}{mK}\right]$ | CALIBRATED CONDUCTIVITY $\left[\frac{W}{mK}\right]$ |
|--|--|--|
| Cerablanket top insulation | ~0.06 | 1.5 |
| Rockwool side and bottom insulation | ~0.09 | 0.35 |

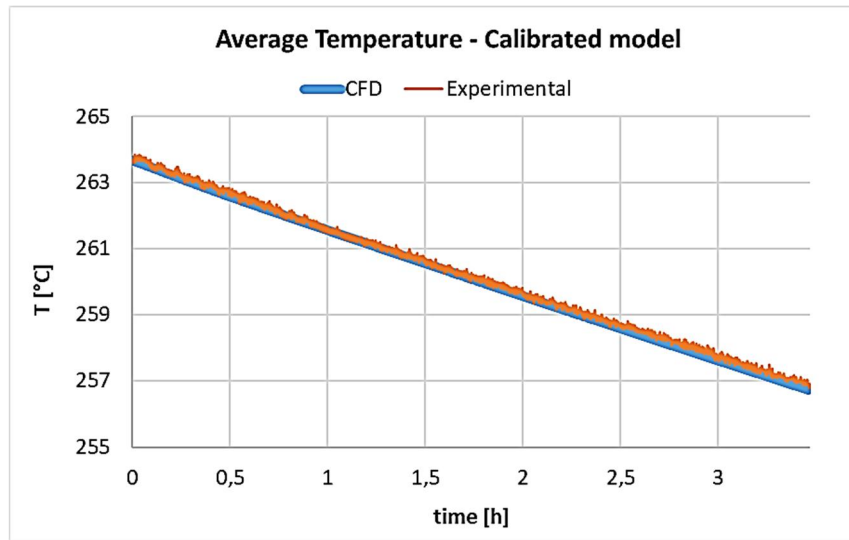


Figure 3.11 Average MS temperature comparison with equivalent thermal conductivities

3.7 Benchmark

The capability of the set of models listed in *section 3.4* to accurately solve problems driven mainly by buoyancy forces, like the one under exam in this work, is verified through some *benchmark cases*, for which either an analytical solution is possible or verified results are available.

3.7.1 U-Shaped Tube with Analytical Equivalent

A U-shaped tube configuration with the same diameter and height of the real internal channel was ideated (*Figure 3.12*), in order to mimic the same chimney effect mechanism that causes the molten salts motion in a simpler geometry, for which an analytical equivalent was possible. To do so, a 3D stationary CFD simulation of this U-shaped tube was carried out imposing the inlet temperature $T_{in} = 200^{\circ}\text{C}$ and a heat load typical of the real charge tests ($\dot{Q} = 30 \text{ kW}$) in a region corresponding to the charge HX (orange rectangle), obtaining an *average MS velocity* of $\bar{V}_{CFD} = 0.15 \text{ m/s}$. The analytical equivalent of this

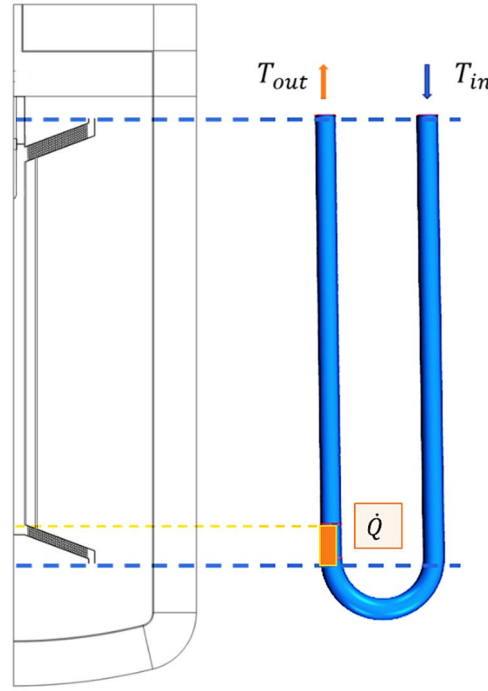


Figure 3.12 U-Shaped tube concept for chimney effect reproduction

situation consists instead in the application of the *Bernoulli Equation* between the inlet and outlet section of the U-shaped tube, coupled with a simple power balance on the region where the volumetric heat source is located. The pressure drops are evaluated through the methodology proposed by Shah in [32] for the distributed laminar entry length fluxes of the two straight branches, while a concentrated pressure loss coefficient K_L equal to 1.5 for 180° return bends [33] is applied for the curve.

$$\begin{aligned}
 p_{in} + \rho_{in}(T_{in})gz_{in} + \frac{1}{2}\rho_{in}(T_{in})V_{in}^2 \\
 = p_{out} + \rho_{out}(T_{out})gz_{out} + \frac{1}{2}\rho_{out}(T_{out})V_{out}^2 + \Delta p_{losses}
 \end{aligned} \tag{3.7}$$

$$\Delta p_{losses} = \Delta p_{distributed} + \Delta p_{curve} \tag{3.8}$$

$$T_{out} = T_{in} + \frac{\dot{Q}}{\dot{m}_{MS} c_{p,MS}} \quad (3.9)$$

$$V_{out} = V_{in} \frac{\rho_{in}}{\rho_{out}} \quad (3.10)$$

This system of equations was solved *iteratively* obtaining a good agreement between the analytical and the CFD solution.

$$V_{in} \cong V_{out} = 0.149 \text{ m/s} \cong V_{CFD}$$

3.7.2 Verification Against Experimentally Verified Data

In this case, the CFD results are compared against the numerical model developed in the DYNASTY Project [34, 35], which is validated against experimental data. The geometry is similar to the one of the previous section, but in this case the power is provided to the molten salts uniformly in the whole domain. Even in this case, coherent results have been obtained in terms of mass flowrate:

Table 3.4 Comparison with the DYNASTY results

| PROVIDED POWER [kW] | REFERENCE VALUES [34, 35] [kg/s] | PRESENT MODEL [kg/s] |
|------------------------|-------------------------------------|-------------------------|
| 10 | 0.28 | 0.27 |
| 0.5 | 0.062 | 0.064 |

3.7.3 ENEA Preliminary CFD Model

During the design phase, ENEA also developed a slightly simplified CFD model using the software *Ansys Fluent*. A computational domain including only the MS was considered, with all the surfaces considered adiabatic, apart from the one of the charge HX, where a constant power of 6.25 kW was provided for a transient simulation with the duration of 3800 s, starting from a uniform tank temperature of 195°C. The same simulation was implemented in the present model, and the results are compared by means of the temperature distribution maps at the end of the transient.

Figure 3.13 shows that the resulting thermal stratification computed by the two models is almost the same.

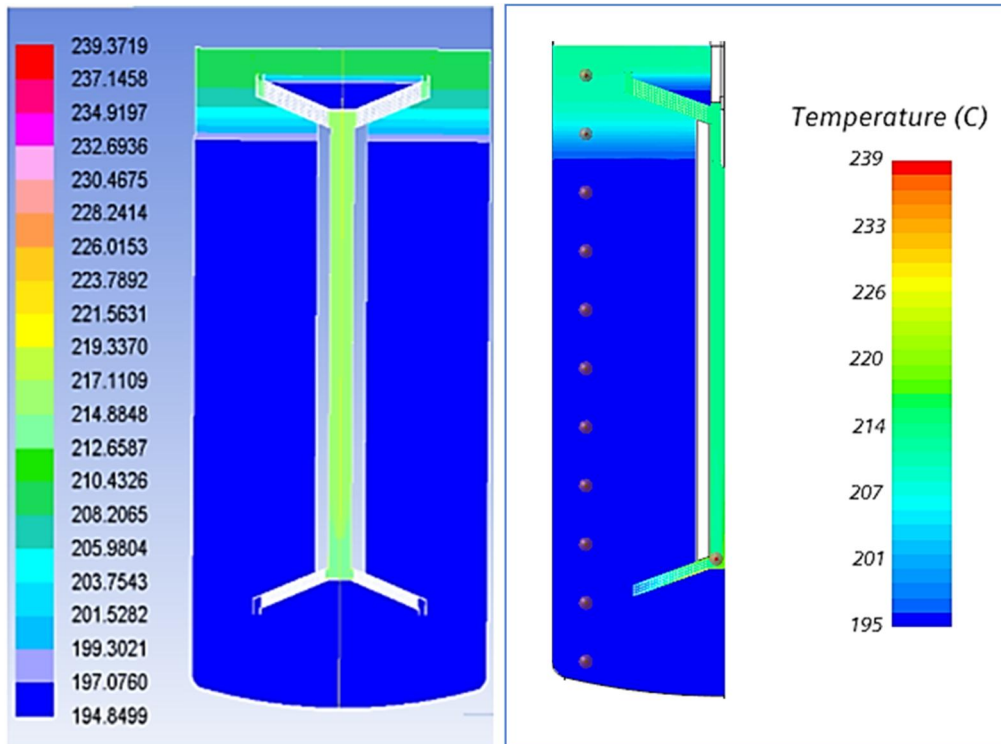


Figure 3.13 ENEA Ansys outcome (left) and present model outcome (right)

Chapter 4

4. Validation of the Model

Once the model has been entirely defined and presented, the following step is the simulation of the real transients, available from the experimental data, and the comparison of the CFD outcome with what was actually measured. If not differently specified, in all the simulations that follow, the boundary and initial conditions have been set with the modalities introduced in *section 3.3*, starting from the experimental data available for the test under exam, and will not be furtherly discussed.

4.1 Comparison with Experimental Data

The comparison with the experimental data of the outcomes of the CFD model as it was presented in the previous sections (i.e. relative to the design geometry of the tank) was not good at all. One representative case is now reported, from which the main differences can be analysed, and some corrections can be developed.

In particular, the outcome of the CFD simulation of a transient belonging to the *charge test 1* is now going to be presented: from minute 80 to minute 120 (highlighted in yellow in *Figure 4.1*), with almost stationary load conditions and impeller switched off. *Figure 4.2* shows the resulting stratification temperature after 2400 seconds, at the end of the transient, comparing it with the experimental one. The difference is clear and evident: while during the test the tank experiences an almost uniform, but low, temperature increase, the CFD simulation provides a result in which the 3 highest thermocouples have a much bigger increment, almost 30°C more.

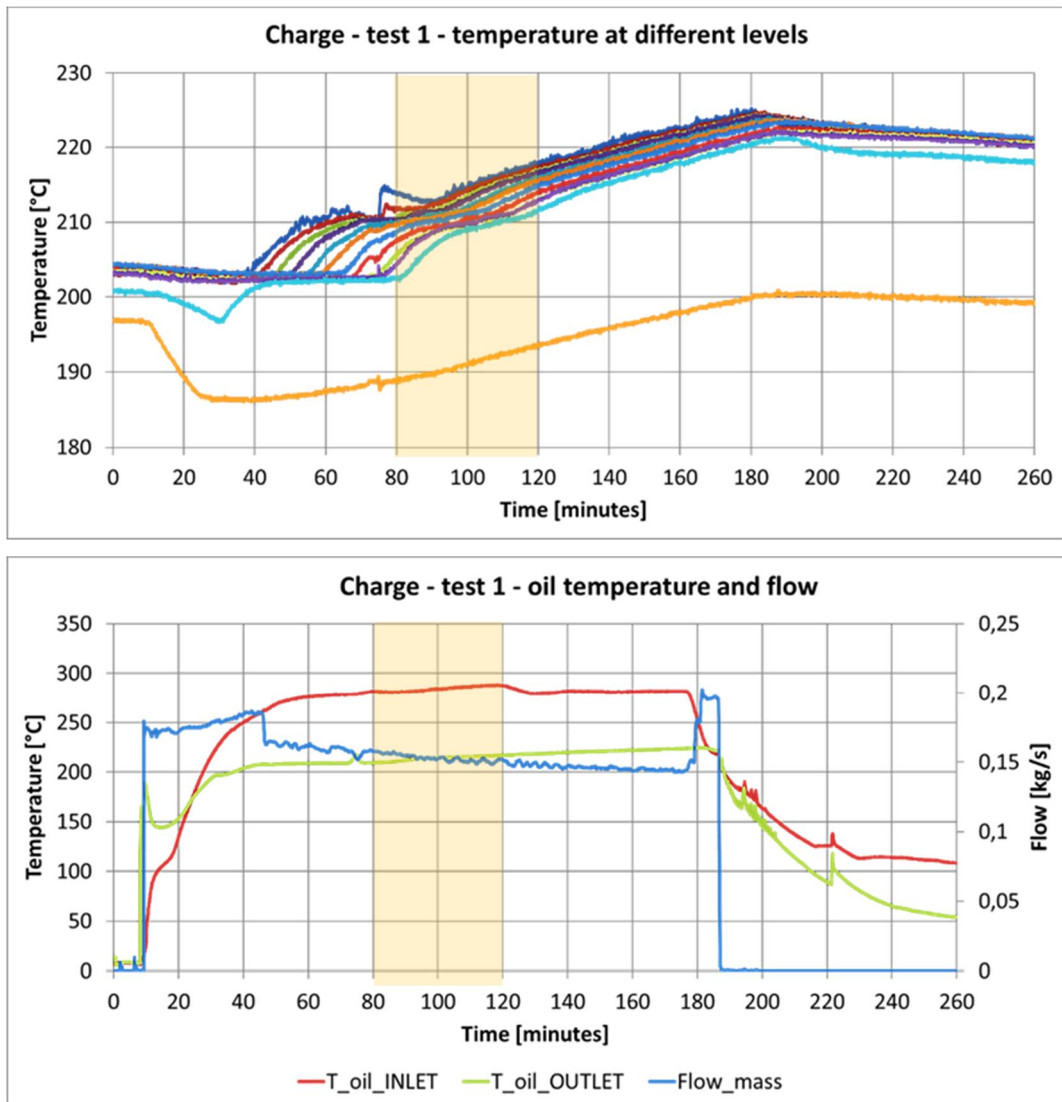


Figure 4.1 Simulated transient (highlighted in yellow) from charge test 1

It can be noticed that the thermocline performance predicted by the CFD is much better in terms of storing efficiency (see *section 1.3.2*), because of the higher temperature difference between the top and the bottom of the tank and an appreciable thermocline

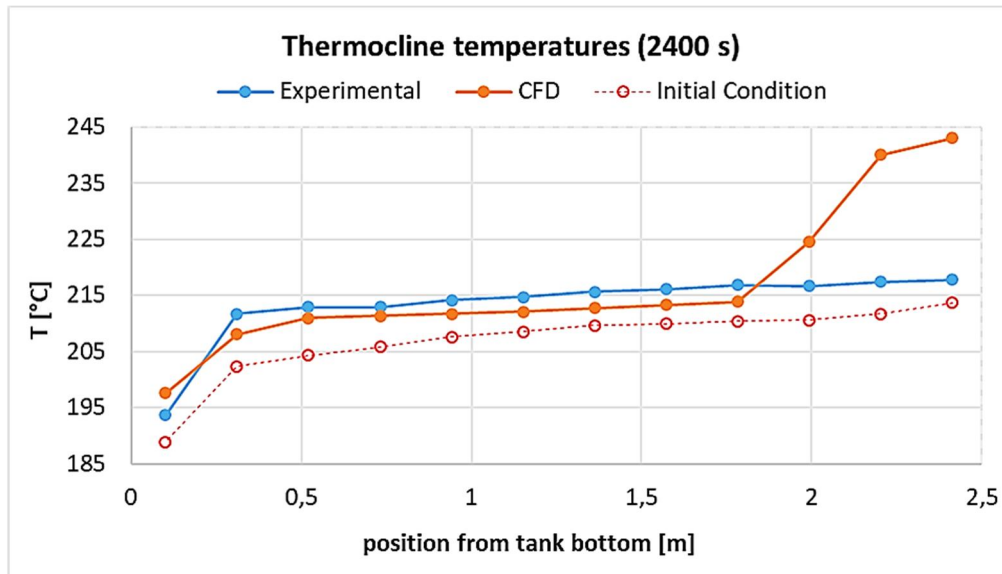


Figure 4.2 Thermocline temperatures comparison at the end of the transient

zone around the height of 2 m. This problem was also noticed by ENEA during the experimental campaign and, as stated in [24], *it may be due to a too high molten salts mass flowrate in the channel*.

Hence, a comparison between the mass flowrates in the two cases can be set: we know that the experimental MS mass flowrate can only be *estimated* through a simplified power balance between oil and salts on the internal channel (*equation (2.1)*), whilst from the CFD simulation a direct and precise report can be easily obtained.

| INTERNAL CHANNEL MASS FLOWRATES COMPARISON | |
|--|-------|
| EXPERIMENTAL [kg/s] | ~ 3 |
| CFD [kg/s] | ~ 0.7 |

In fact, the mass flowrate measured in the CFD model, for the same transient, is *almost 5 times lower* with respect to the experimental estimation. This problem needs to be further analysed, also because, as shown in *Figure 4.3*, in the CFD simulation the heat

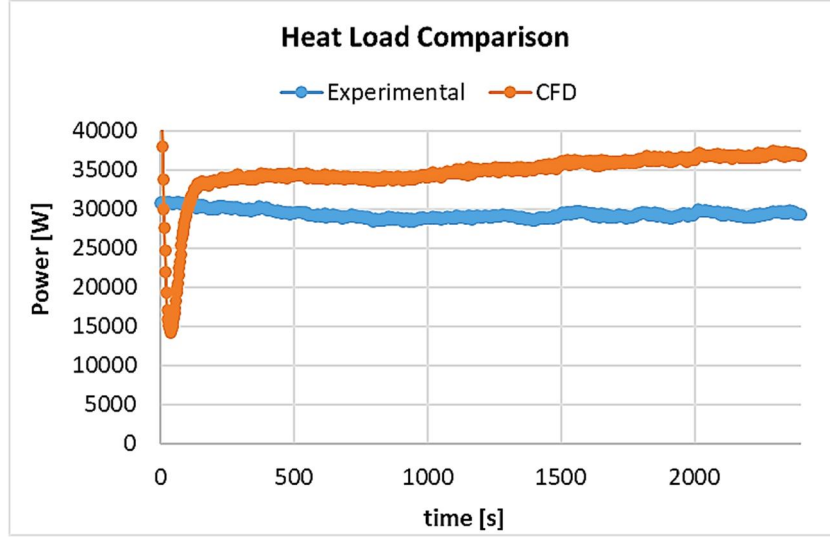


Figure 4.3 Comparison of the heat load between experiment and CFD outcome

provided to the molten salts by the charge HX boundary condition is slightly bigger than the experimental one, evaluated as

$$\dot{Q}_{LOAD} = \dot{m}_{oil} \cdot \int_{T_{oil,out}}^{T_{oil,in}} c_{p,oil}(T) \cdot dT \quad (4.1)$$

and then, in principle, the opposite problem should occur, with a bigger mass flowrate triggered in the CFD simulation.

4.2 Analysis of the Problem

The problem may be due to an error in the estimation of the experimental mass flowrate, then *equation (2.1)* is recalled here:

$$\dot{m}_{MS,exp} = \frac{\dot{m}_{oil} \cdot \int_{T_{oil,out}}^{T_{oil,in}} c_{p,oil}(T) \cdot dT}{c_{p,MS} \cdot (T_{MS,out} - T_{MS,in})}$$

The one possibility that is firstly discussed is that the experimental mass flowrate could be very overestimated due to the overestimation of the numerator, namely by the overestimation of the heat provided to the molten salts (\dot{Q}_{LOAD}). The hypothesis here is that, provided the fact that the inlet and outlet temperature of the oil are measured on the circuit outside the tank (*section 2.2.2*), a part of the measured temperature drop may take place outside the tank, and then that only a fraction of the power is actually provided to the molten salts in the heat exchanger. An *energy balance* can then be set, comparing the energy received by the molten salts in the tank to the one that is supposed to be provided by the oil during the whole transient.

$$E_{oil} = \sum_{i=1}^{N_{exp}} \left(\dot{m}_{oil,i} \cdot \Delta t_{exp} \cdot \int_{T_{oil,out,i}}^{T_{oil,in,i}} c_{p,oil}(T) \cdot dT \right) \quad (4.2)$$

$$E_{MS} = \sum_{i=2}^{N_{exp}+1} [M_{tot,MS} \cdot c_{p,MS} \cdot (T_{avg,MS,i} - T_{avg,MS,i-1}) - \dot{Q}_{losses} \cdot \Delta t_{exp}] \quad (4.3)$$

where N_{exp} is the number of experimental data collected each timestep $\Delta t_{exp} = 5$ s, the total mass of the molten salts inside the tank is $M_{tot,MS} = 5288$ kg and the value of 4 kW was considered for \dot{Q}_{losses} , from *section 3.6*. As the time cumulated value of these two quantities shows in *Figure 4.4*, they are perfectly balanced, and consequently this hypothesis must be discarded.

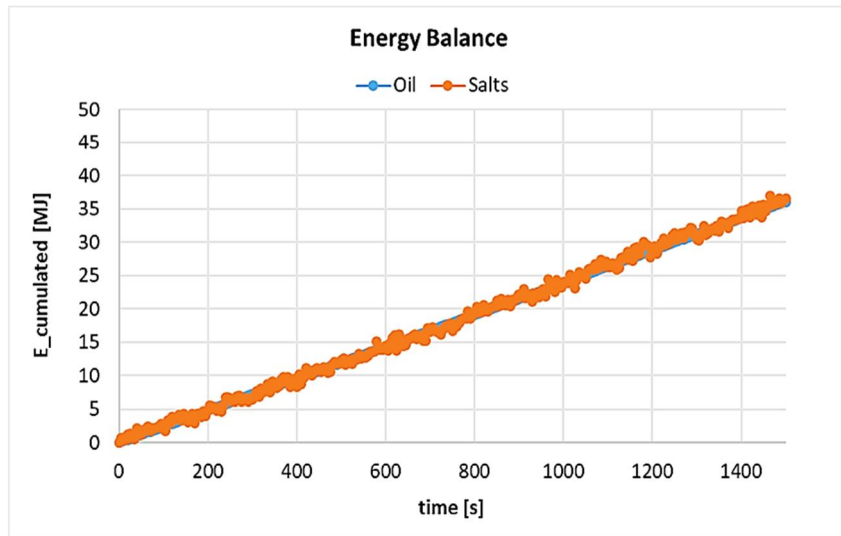


Figure 4.4 Comparison of the energy cumulated of oil and tank molten salts

So, the difference between the experimental mass flowrate and the CFD one is very likely to be real, and then

- ❖ verified the capability of the model to reproduce buoyancy driven phenomena (section 3.7);
- ❖ provided that the prototype behaviour was not satisfactory, and in any case was very different from the predicted one;
- ❖ provided that the CFD model is based on the design drawings of the prototype and that the definitive constructive drawings are not available:

the hypothesis that this evident difference is due to an internal configuration of the tank different from the one designed, has been made.

In particular, the hypothesis is that for some reason a *preferential path* with lower pressure drops for the molten salts is present in the channel, causing a very high mass flowrate and not allowing the good operation of the thermocline.

4.3 Modification of the Geometry

There is no way to know the precise conformation of this supposed preferential path. In accordance with ENEA, a *problem in the coupling between the different parts* of the internal channel is considered as the most likely option. The internal channel is in fact made out of three main blocks: the discharge HX and the charge HX with their respective enclosures, and the vertical section that connects them. These blocks are then connected one another and inserted in the tank from the top as a whole, so that the possibility is that something went wrong either in the assembling or in the positioning, creating what can be called as a sort of *bypass* that allows the passage of a high quantity of molten salts in parallel to the heat exchangers. This is shown in **Figure 4.5**, with a bypass created *below* the discharge HX, and one created *above* the charge HX, that will be assumed of the same thickness, for the sake of simplicity.

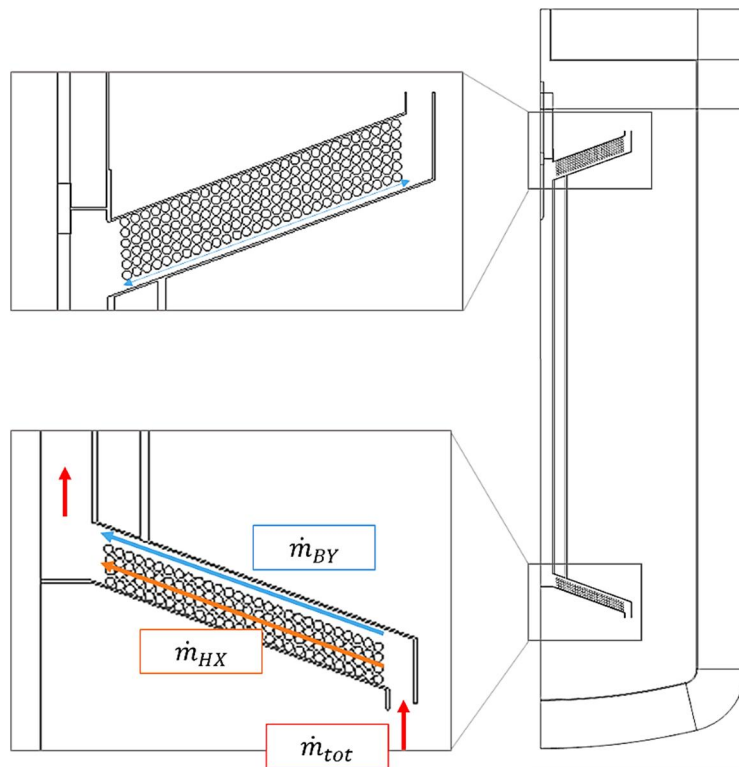


Figure 4.5 Modified geometry with 'bypass' on the heat exchangers

4.3.1 Parametric Analysis on the Bypass Thickness

Some CFD simulations of the same charge transient considered in *section 4.1* have been performed, measuring the resulting total mass flowrate, the fraction of it that passes through the HX and those that conversely bypasses it, as shown in *Figure 4.5*. The process of geometry modification and implementation in the CFD software is very long, then only 3 different thicknesses have been actually simulated, and the other results have been extrapolated by means of a ‘best fit’ curve. The plot in *Figure 4.6* shows, for the different configurations, the two fractions of the total mass flowrate, alongside with the power provided to the molten salts by the Robin boundary condition at the heat exchanger. In particular, as the thickness of the bypass increases, the share of the mass flowrate that bypasses the heat exchanger increases too. A problem is due to the fact that, as the quantity of molten salts passing through the HX decreases, also the power provided to them decreases, and it is in any of the simulated case smaller than 30 kW, which is the

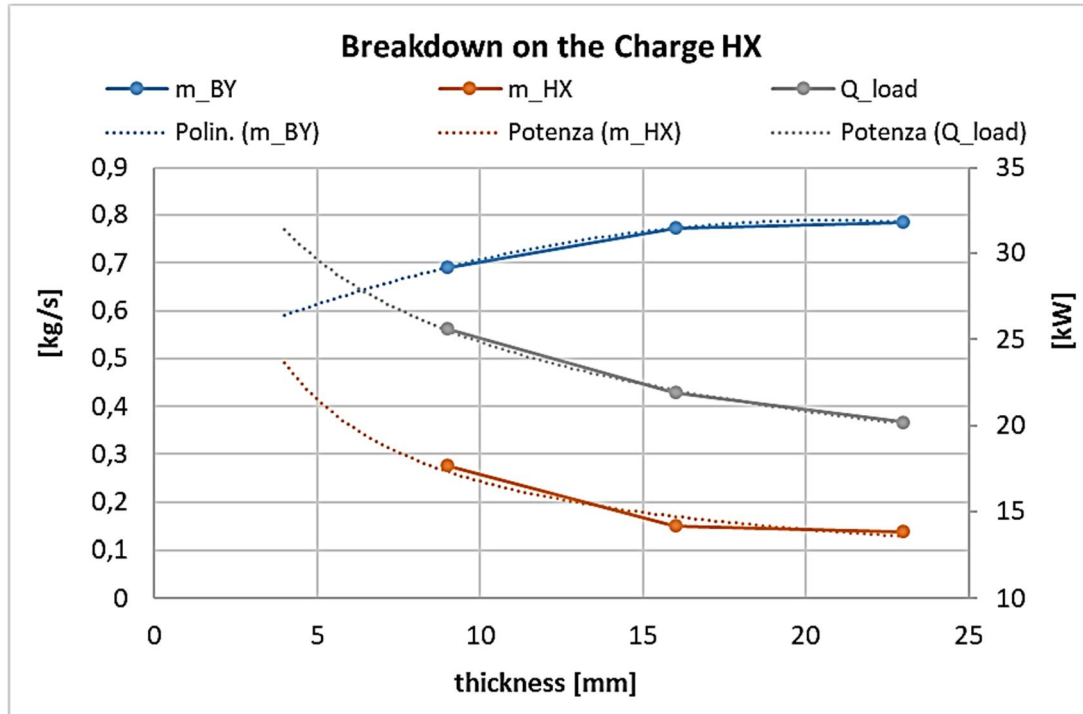


Figure 4.6 Mass flowrate and power analysis on the HX, varying the thickness of the bypass

experimental load measured in this test, as previously presented in **Figure 4.3**. Following the dotted trend lines, such power would correspond to a bypass thickness of 5 mm, for which the total mass flowrate would be, from the plot:

$$\dot{m}_{tot,5mm} = \dot{m}_{BY,5mm} + \dot{m}_{HX,5mm} = 0.6 + 0.4 = 1 \text{ kg/s}$$

which still is too low for the purpose of matching the experimental data. The deduction from this is that the *heat load boundary condition* as it was ideated, *is no more adequate for reproducing the phenomenon* in this modified configuration. This BC was presented under the hypothesis of uniform heat flux, which certainly falls with the introduction of a bypass that creates regions with very different mass flowrates. Moreover, it would be very difficult to adjust such a sophisticated boundary condition provided the fact that, with the real geometry in principle unknown, some *fin effects* due to possible contacts between the different serpentine or between a serpentine and the shell, that may greatly influence the heat exchange, are impossible to be assessed. Consequently, in order to have the confidence of applying a correct heat load, the decision is to **modify the heat load**

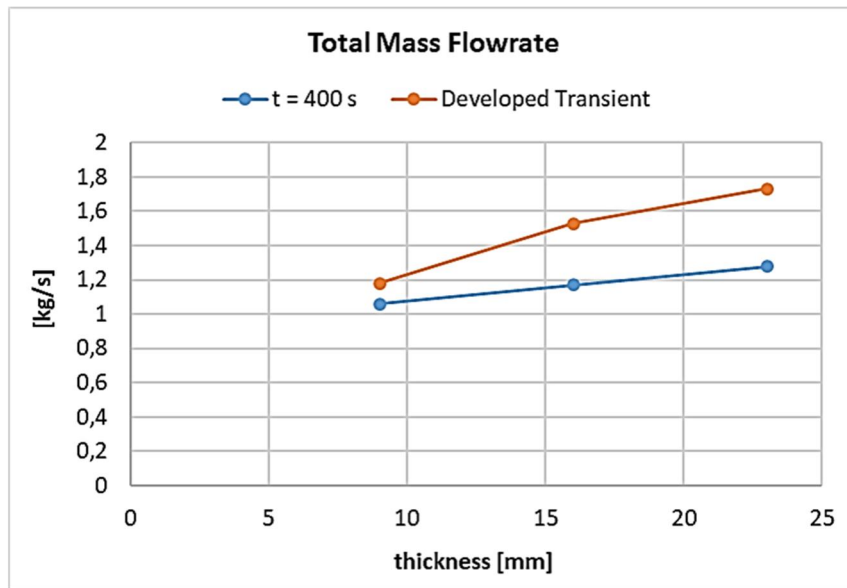


Figure 4.7 Total mass flowrate with the imposed experimental heat load for different thicknesses

boundary condition: from now on, the experimental heat load has been simply applied to the heat exchangers walls as a *heat source*.

With this new BC, the total mass flowrate resulting from the different thickness configurations is reported in *Figure 4.7*. Now, with the correct amount of power provided to the salts in all the cases, the total mass flowrate increases with the bypass thickness, and reaches a particularly interesting value of 1.8 kg/s with a bypass of 23 mm. Despite the experimental *estimation* was of about 3 kg/s, as will be shown in the following sections, this configuration guarantees in many cases a satisfactory reproduction of the experimental data.

4.3.2 Final Model

The only differences between the final model obtained for the reproduction of the experimental data and the model originally developed on the base of the design drawings are summarized in the table below.

Table 4.1 Recap of the model modifications applied for matching the experimental behaviour

| SUBJECT | MODIFICATION |
|--------------------------------------|--|
| Geometry of the computational domain | Application of a 23mm bypass on the charge and discharge HXs |
| Heat load BC | Experimental load directly applied as <i>heat source</i> |

Figure 4.8 shows the great improvement with respect to the results of the original model (*Figure 4.1*) regarding the selected transient from *charge test 1*: now the peak in the top thermocouple has been eliminated, with the maximum and minimum temperatures matching those experimentally measured. The simulation of more transients, with more detailed comments, is provided in the next section.

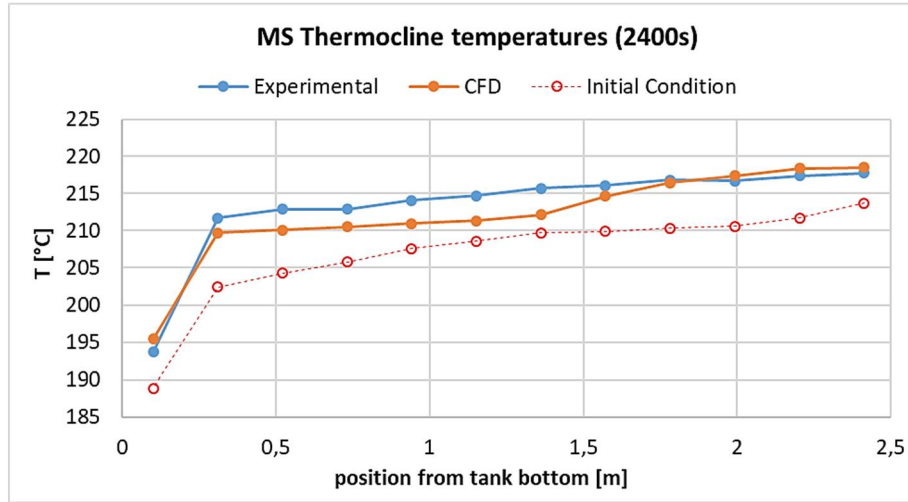


Figure 4.8 Thermocline temperatures comparison with the final CFD model

4.4 Validation of the Final Model

In this section, the results provided by the CFD model in the simulation of a charge and a discharge transient are going to be presented in detail and deeply commented; following these, the results from some other transients will be synthetically reported in *Appendix C*, in a graphical form.

4.4.1 Charge test 2

It is the last charge test chronologically performed: the impeller was never used here, so this transient offers a very long interval of undisturbed data. The simulation was performed from minute 30 to minute 180, as shown in *Figure 4.9*.

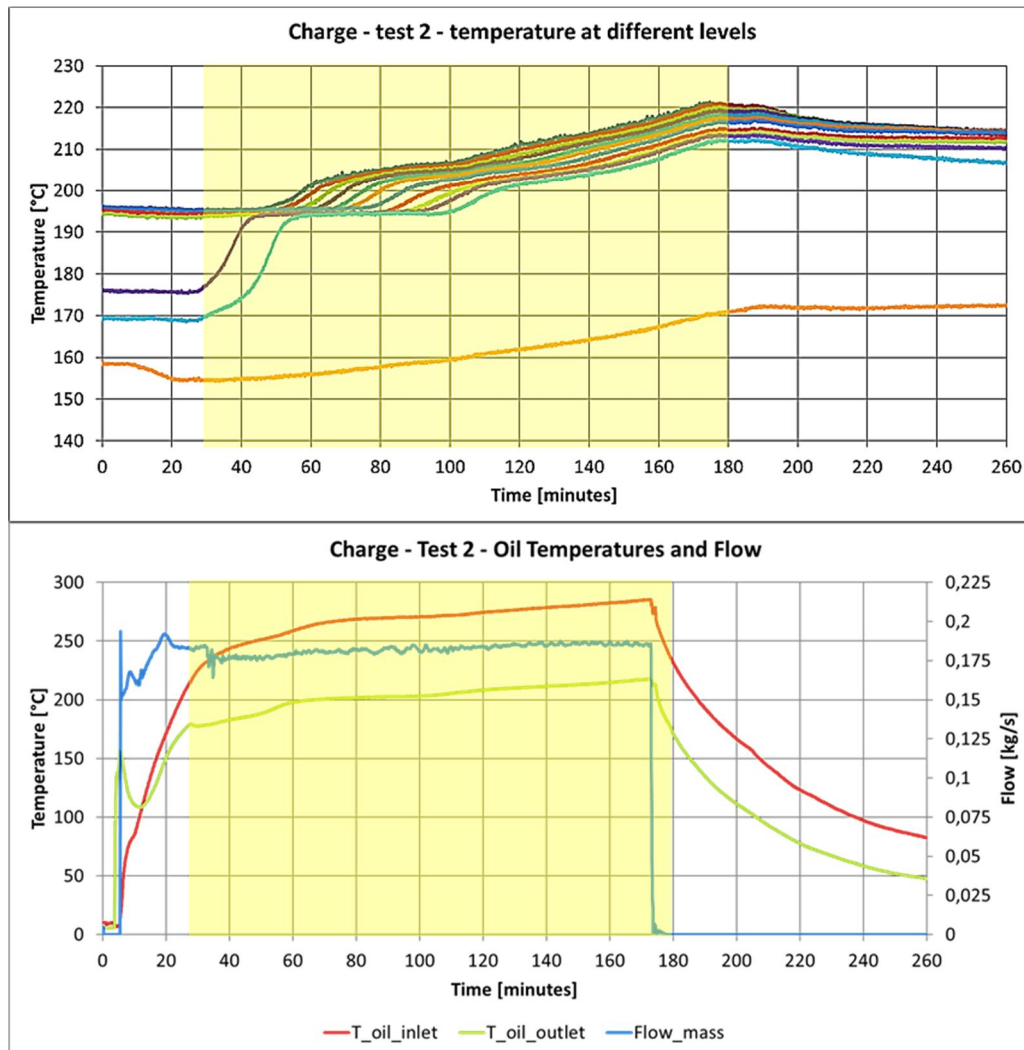


Figure 4.9 Presentation of the simulated transient from charge test 2

The evolution of the temperatures at selected heights from the bottom of the tank is shown in *Figure 4.10*, comparing the outcome of the CFD model with the experimental data. The accordance is quite good for all the thermocouples, but still the measured temperature increases are in slight anticipation with respect to the CFD ones, and eventually,

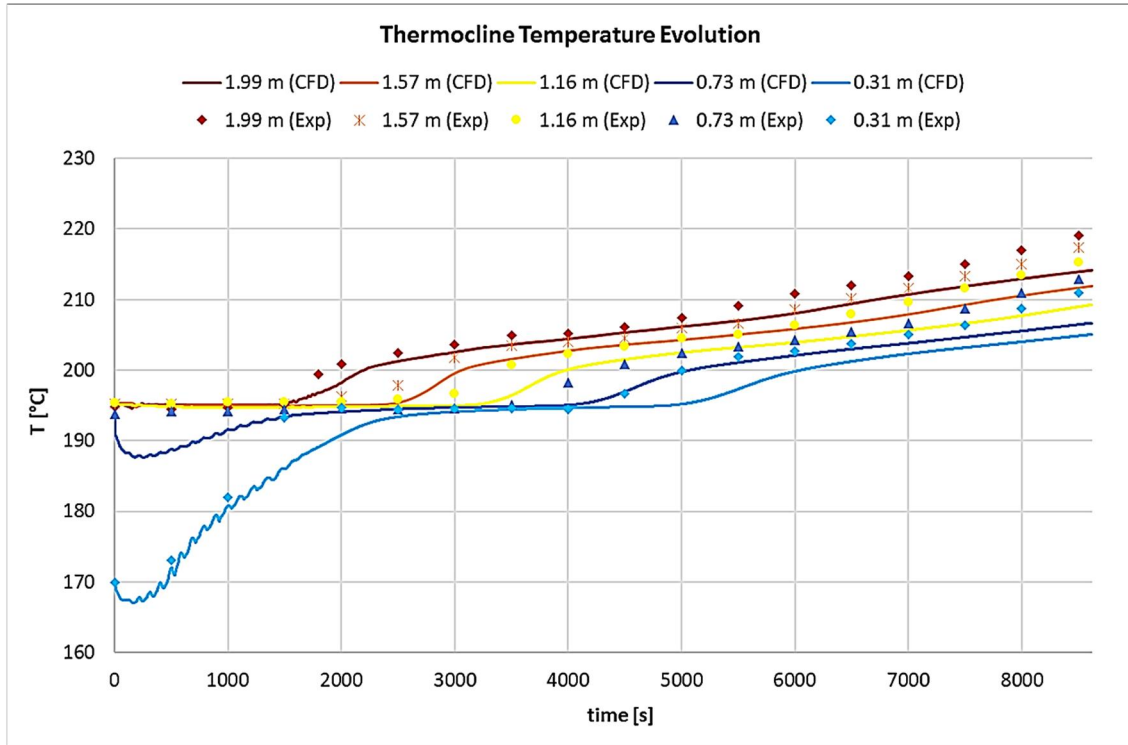


Figure 4.10 Temperature evolution at different heights: CFD and experimental comparison

after a very long transient of almost two and a half hours, reach higher temperatures than those numerically reproduced.

The comparison of the thermocline temperatures at a frozen instant after 1 hour and 20 minutes, shown in *Figure 4.11*, is representative of the good performances of the model in this case. In fact, comparing in the two cases the temperature increments for each thermocouple with respect to the initial condition, an *average relative error* of 17% is obtained, whit a *maximum absolute error* of 5°C and an *average absolute error* of only 2.1°C, concentrated in the lowest thermocouples.

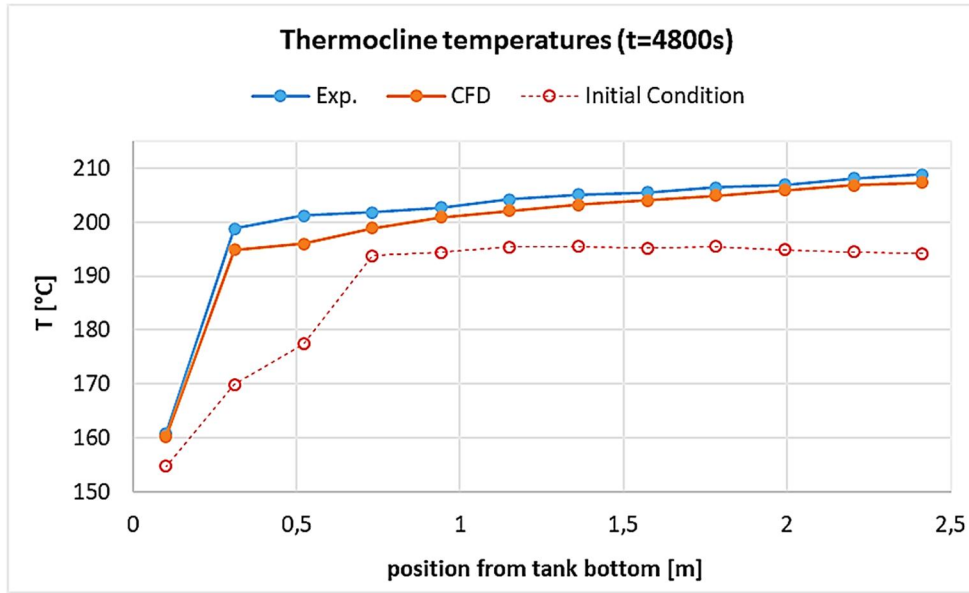


Figure 4.11 Thermocline temperatures after 4800 s of transient

Finally, the temperature and velocity maps after a simulation time of 2400 s are reported in *Figure 4.12*. From here one can appreciate the salts moving in the internal channel, from the bottom, where they are heated up, towards the top of the tank; a magnification of the velocity inside the charge HX is provided too, showing the role of the bypass, where the movement of the molten salts is easier and the highest share of the mass flowrate rises. The vortices in the upper air region can be noticed too, with the cold air entering the domain and the hot one exiting, as also the temperature map shows. This last map also shows the stratification inside the bulk molten salts, the hotter fluid rising up in the internal channel and the role of the external insulation layers, in which a high temperature gradient is set, protecting the molten salts from the cold external temperature.

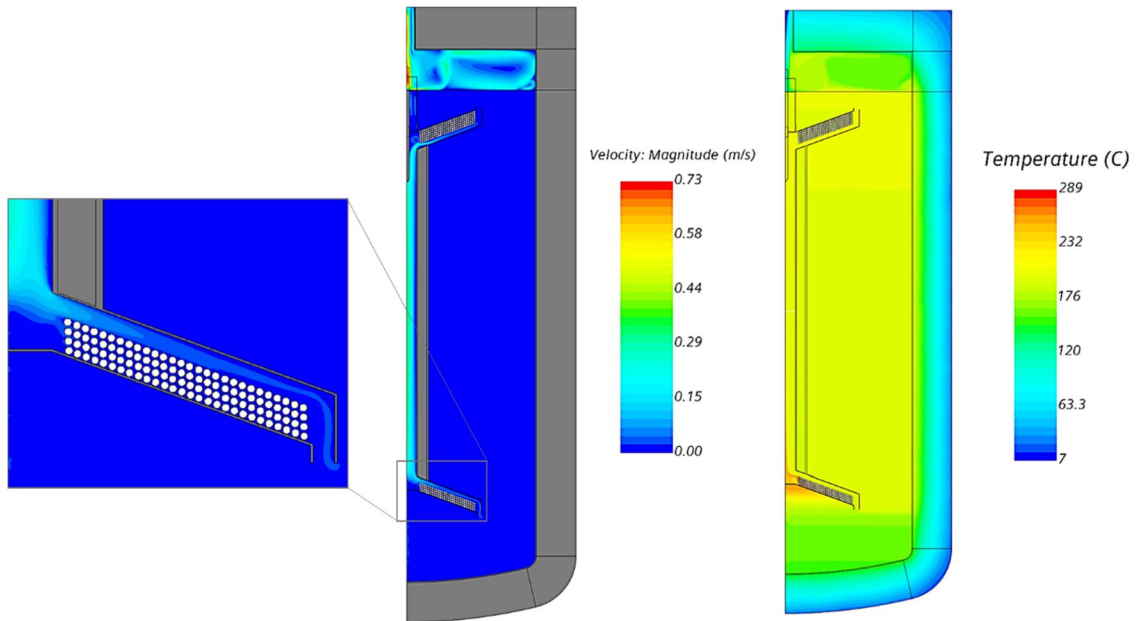


Figure 4.12 Temperature and velocity maps after 2400 s

4.4.2 Discharge test 4: selected transient

Similar considerations are now made about a discharge transient. A shorter transient is now considered since the impeller was used most frequently in discharge transients, and undisturbed transients have now to be considered: from minute 80 to minute 95, with stable discharge conditions on the oil side (*Figure 4.13*).

Again, the temperature evolution at different heights from the tank bottom are compared for the two cases in *Figure 4.14*. The CFD evolution is again slower with respect to the experimental one, suggesting that the experimental mass flowrate in discharge phases is still slightly bigger than the one reproduced in the CFD simulation. At least, the extreme temperatures of the thermocline are reproduced with a good accuracy.

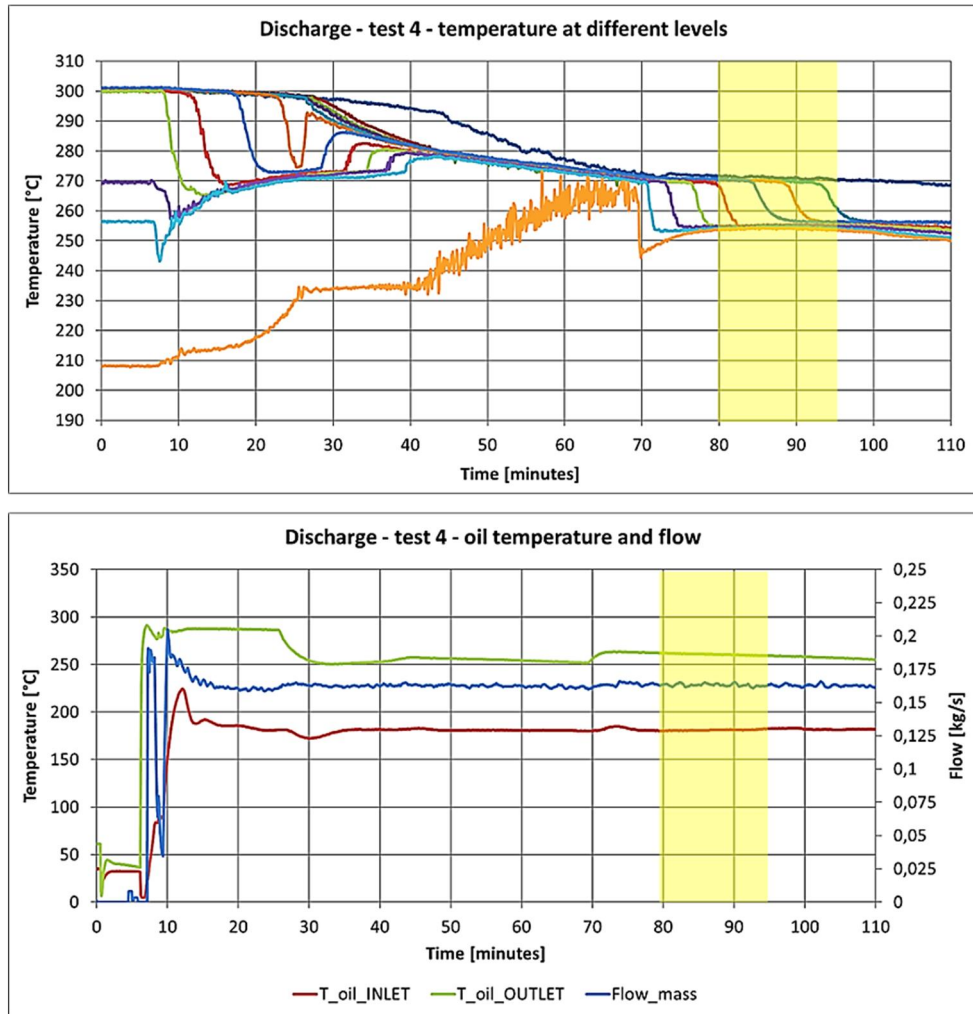


Figure 4.13 Presentation of the simulated transient from discharge test 4

Examining the thermocline temperatures for the 4 central thermocouples at the end of this transient (*Figure 4.15*), and considering their temperature variations with respect to the initial conditions, an *average relative error* of the 23% is computed, which is maximum (40%) for the thermocouple at a height of 1.6 m, where the *absolute error* is of 4.3°C with respect to an experimental decrement of 10.6°C.

In *Figure 4.16* are instead reported the temperature and velocity maps for this discharge case. The molten salts moving downwards, with a detail on the zone of the

discharge HX bypass, can be appreciated, as well as the temperature stratification at a higher temperature with respect to the previous case.

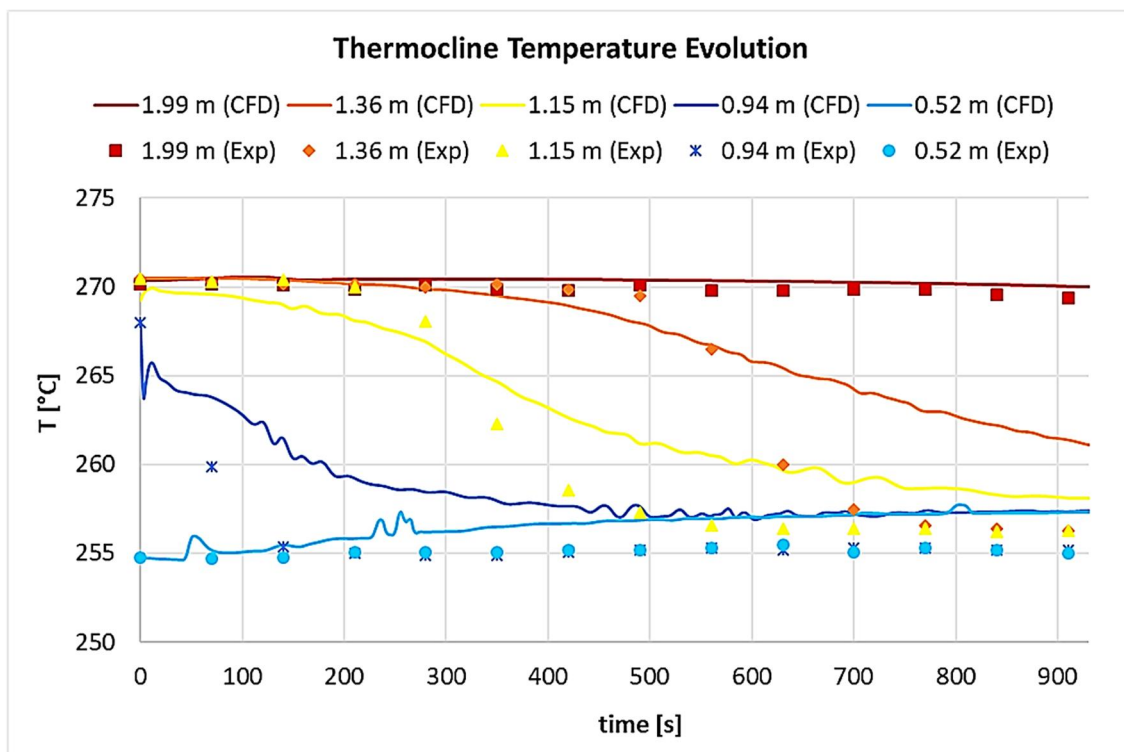


Figure 4.14 Temperature evolution at different heights: CFD and experimental

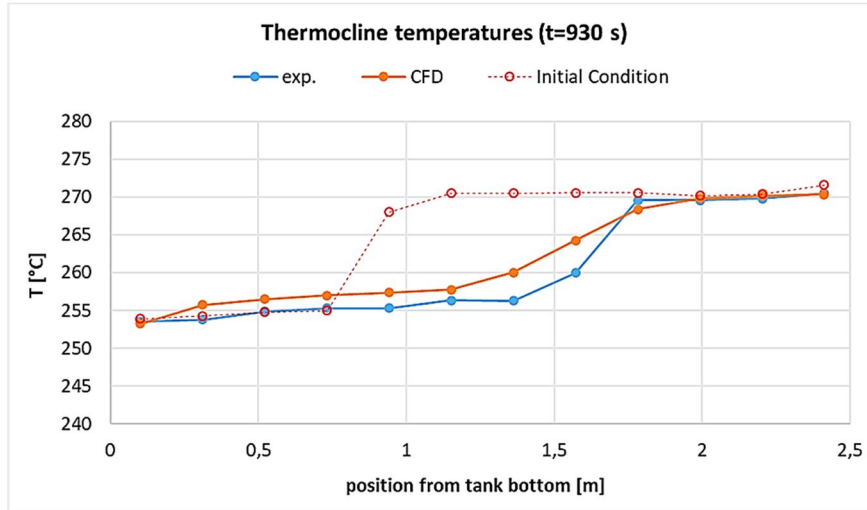


Figure 4.15 Thermocline temperatures after a transient of 930 s

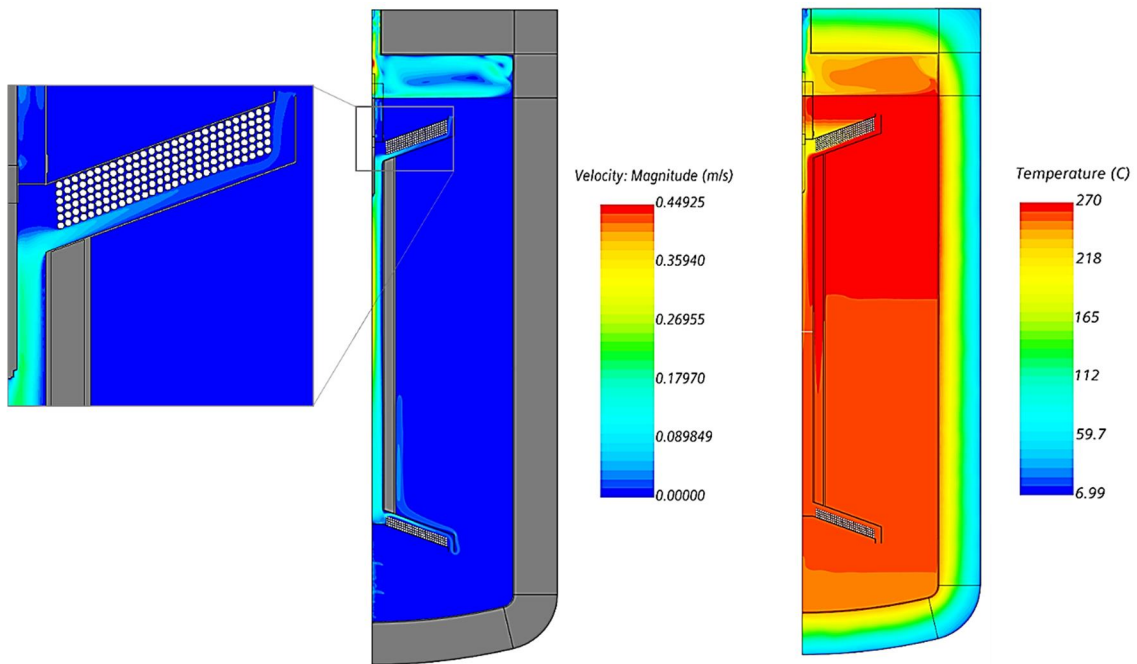


Figure 4.16 Temperature and velocity maps at the end of discharge transient 4

Other results are synthetically reported in graphical form in *Appendix C*.

Chapter 5

5. Conclusions and Perspective

In this work a CFD model has been developed, able to reproduce the transient behaviour of the prototype of innovative thermocline thermal energy storage designed by ENEA, with two integrated heat exchangers connected by an internal channel. As demonstrated by the validation presented in the previous chapter, this CFD model, produced using the commercial software *STAR-CCM+*, ensures a sufficient accuracy, especially for the charge transients, with a computational cost that has been kept low by using a 2D axisymmetric computational domain.

At first, the numerical and experimental results were not in good agreement. The cause of this problem was identified in the different molten salts mass flowrate that flows in the channel, even with a heat load that was verified to be comparable between the CFD model and the actual one. The deduction was then that the geometry of the prototype could be somehow different from the designed one initially implemented in the model: it is a plausible option, since only the design drawings are available for the tank, not the final drawings. In particular, a configuration that provides to the molten salts a preferential path, with lower pressure drops, would explain the behaviour of the prototype. Unfortunately, there was no practicable way to open the tank detecting the actual nature of this difference from the design. Therefore, a possible new geometry was *assumed*, namely the presence of a bypass above the charge HX and below the discharge HX, of an equal thickness determined by means of a parametric analysis. Finally, the results of this modified model have been compared also with experimental tests different and independent from the one used for the parametric analysis, showing very good performances with charge

transients and acceptable accuracy also in reproducing discharge transients. In particular, it is possible that during discharge transients the molten salts mass flowrate was still slightly bigger than the one that the model with the assumed geometry is able to reproduce.

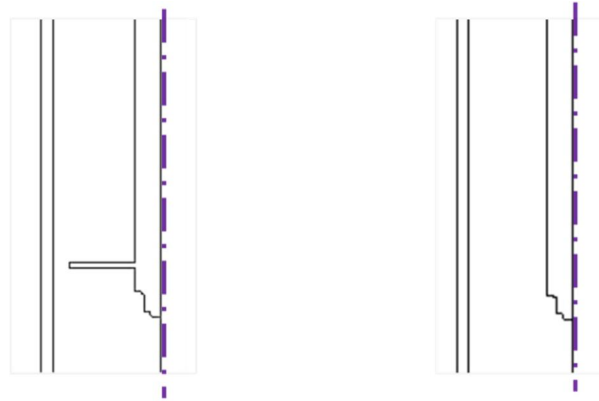
Thus, it can be stated that the final model has been successfully validated against the experimental data, and it can potentially be used for the evaluation of the effectiveness of possible improvements to be applied to the concept. In fact, the efficiency of this prototype is still not satisfactory, because the salts mass flow rate in the internal channel is too high and does not permit the formation of an appreciable stratification within the tank, neither in charge nor discharge phases. In this sense, the design geometry would have already provided better results, as it was shown with the original model, where the stratification of the computed transient was much more evident, and the maximum temperature obtained was almost 30°C higher with respect to the experimental one. Furthermore, the possible benefits coming from the insertion of some *phase changing materials* (PCM) within the tank, for exploiting also the *latent heat storage*, will be assessed with the help of the validated model.

Appendices

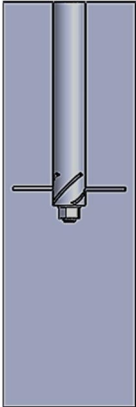
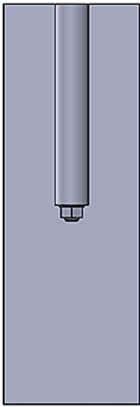
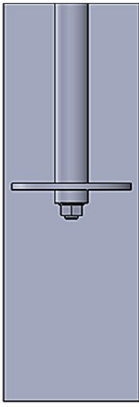
Appendix A

Impeller Bidimensional Axisymmetric Representation

In order to assess the best way to reproduce the effect of the impeller on the molten salts flux in the bidimensional axisymmetric domain, the two extreme cases have been considered for the sake of simplicity: one with the profile of the entire blade (left) and one without the blade profile (right).



Some simple 3D CFD simulations have then been performed, imposing a mass flowrate of 1 kg/s of molten salts in a section of the internal channel, containing respectively the real 3D profile of the impeller and the 3D representations of the two axisymmetric profiles, in order to evaluate the resulting *pressure drop*.

| REAL IMPELLER SHAPE | NO BLADES | 360° BLADE PROFILE |
|--|--|--|
| NOT Axisymmetric | Axisymmetric | Axisymmetric |
|  |  |  |
| $\Delta p = 12 \text{ Pa}$ | $\Delta p = 5 \text{ Pa}$ | $\Delta p = 129 \text{ Pa}$ |

Provided that the *entire blade profile* configuration overestimates by 1 order of magnitude the effect of the real impeller shape, and that the *no blade profile* differs instead just from a factor 2.4 from the real one (only by 7 Pa in absolute terms), the latter has been selected for the definition of the computational domain.

Appendix B

Thermophysical Properties of the Materials

HITEC XL[®]

Private Communication: material characterization carried out in ENEA laboratories [1]

AIR

| | | |
|----------------------|--|---|
| Specific Heat | $c_{p,air} \left[\frac{J}{kgK} \right]$ | $1042.5 - 0.366 \cdot T[K] + 0.00097 \cdot T^2[K] - 6.595 \cdot 10^{-7} \cdot T^3[K] + 1.467 \cdot 10^{-10} \cdot T^4[K]$ |
| Thermal Conductivity | $k_{air} \left[\frac{W}{mK} \right]$ | $0.0013 \cdot T[K] + 9.28 \cdot 10^{-5} \cdot T[K] - 3.301 \cdot 10^{-8} \cdot T^2[K] + 6.52 \cdot 10^{-12} \cdot T^3[K]$ |
| Dynamic Viscosity | $\mu_{air} [Pa \cdot s]$ | $3.83 \cdot 10^{-6} + 5.578 \cdot 10^{-8} \cdot T[K] - 2.294 \cdot 10^{-11} \cdot T^2[K] + 4.935 \cdot 10^{-15} \cdot T^3[K]$ |

DELCOTERM® SOLAR E 15

Source: <https://www.delcosrl.com/it/fluidi-diatermici/delcoterm-solar-e-15>

| | | |
|----------------------|--|--|
| Specific Heat | $c_{p,oil} \left[\frac{J}{kgK} \right]$ | $3.7 \cdot T[^\circ C] + 1805$ |
| Thermal Conductivity | $k_{oil} \left[\frac{W}{mK} \right]$ | $-7 \cdot 10^{-5} \cdot T[^\circ C] + 0.136$ |
| Dynamic Viscosity | $\mu_{oil} [Pa \cdot s]$ | $7.8734 \cdot T[^\circ C]^{-1.754}$ |
| Density | $\rho_{oil} \left[\frac{kg}{m^3} \right]$ | $-0.6686 \cdot T[^\circ C] + 838.67$ |

AISI 316

Source: Atlas Steels

| | | |
|----------------------|---|---|
| Specific Heat | $c_{p,st} \left[\frac{J}{kgK} \right]$ | 500 |
| Thermal Conductivity | $k_{st} \left[\frac{W}{mK} \right]$ | $0.013 \cdot T[K] + 11.449$ |
| Density | $\rho_{st} \left[\frac{kg}{m^3} \right]$ | $\frac{8000}{(1 + 16.2 \cdot 10^{-6} T[^\circ C])}$ |

ROCKWOOL

Source: ProRox[®] WM 950^{ES}

| | | |
|----------------------|---|--|
| Specific Heat | $c_{p,RW} \left[\frac{J}{kgK} \right]$ | 840 |
| Thermal Conductivity | $k_{RW} \left[\frac{W}{mK} \right]$ | $0.0916 - 5.6 \cdot 10^{-4} \cdot T[K] + 1.55 \cdot 10^{-6} \cdot T^2[K] - 9.35 \cdot 10^{-10} \cdot T^3[K]$ |
| Density | $\rho_{RW} \left[\frac{kg}{m^3} \right]$ | 80 |

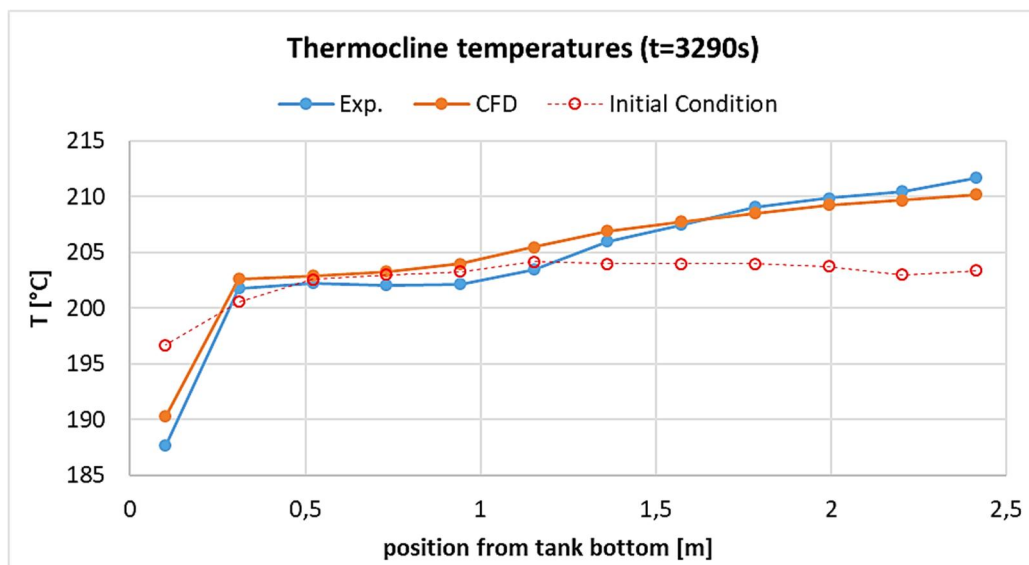
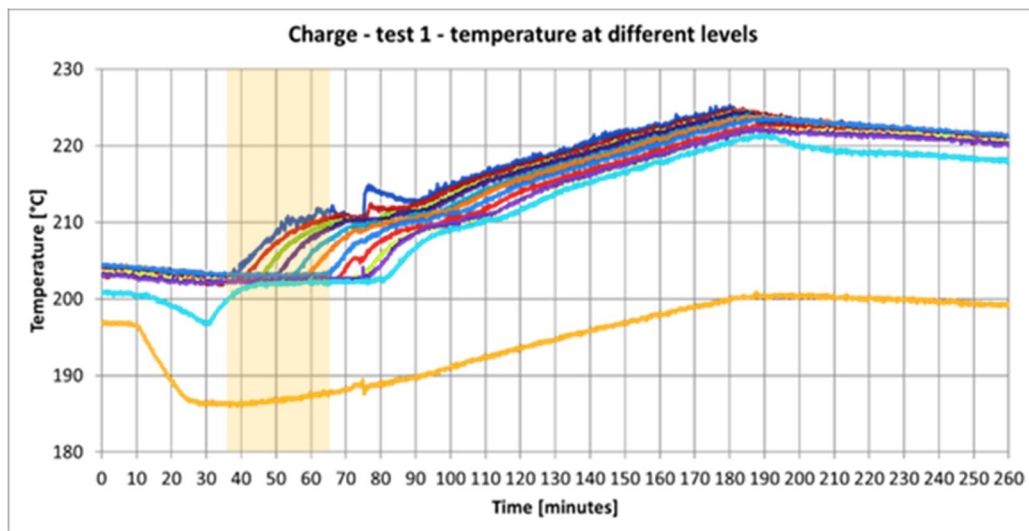
CERABLANKET

Source: Morgan Advanced Materials

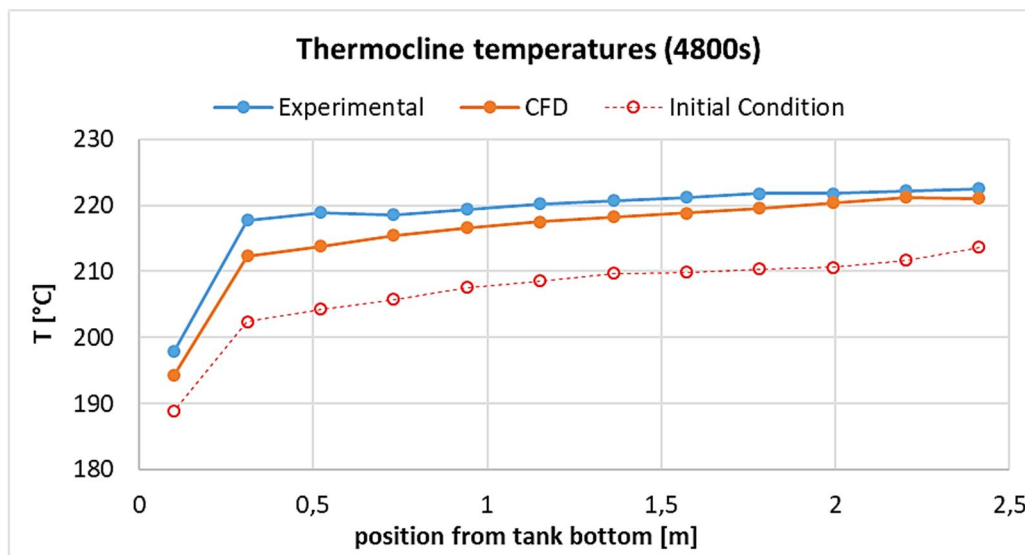
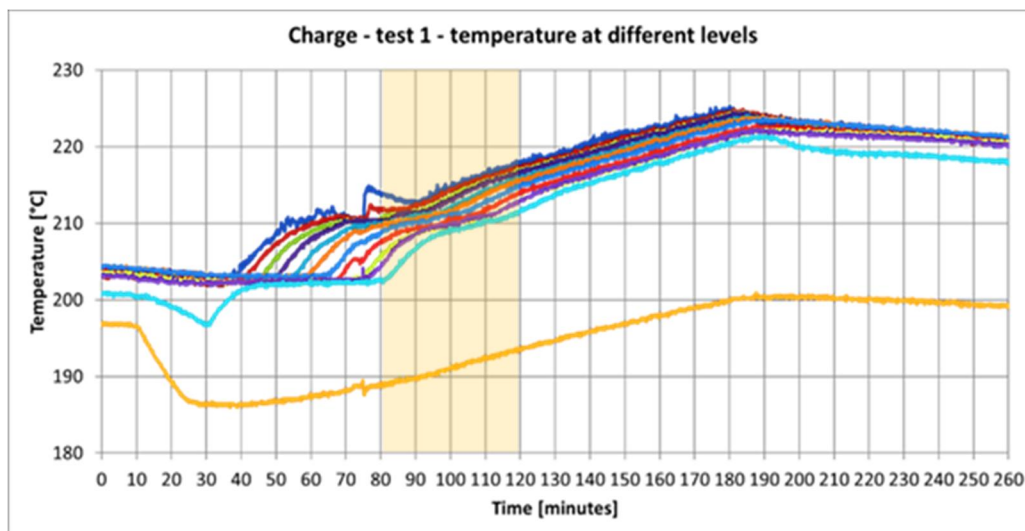
| | | |
|----------------------|---|--|
| Specific Heat | $c_{p,CB} \left[\frac{J}{kgK} \right]$ | 1130 |
| Thermal Conductivity | $k_{CB} \left[\frac{W}{mK} \right]$ | $-0.237 + 8.81 \cdot 10^{-4} \cdot T[K] - 7.54 \cdot 10^{-7} \cdot T^2[K] + 3 \cdot 10^{-10} \cdot T^3[K]$ |
| Density | $\rho_{CB} \left[\frac{kg}{m^3} \right]$ | 128 |

Appendix C

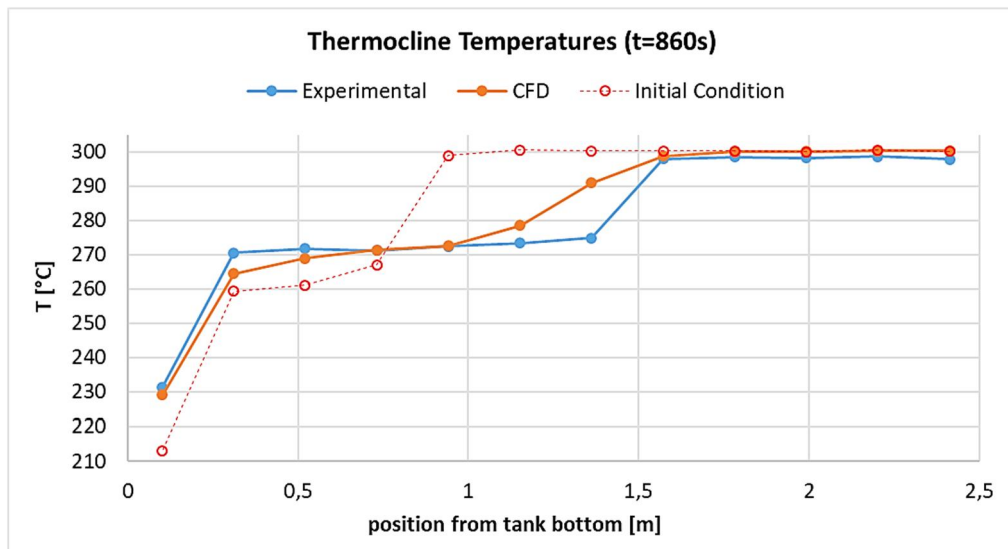
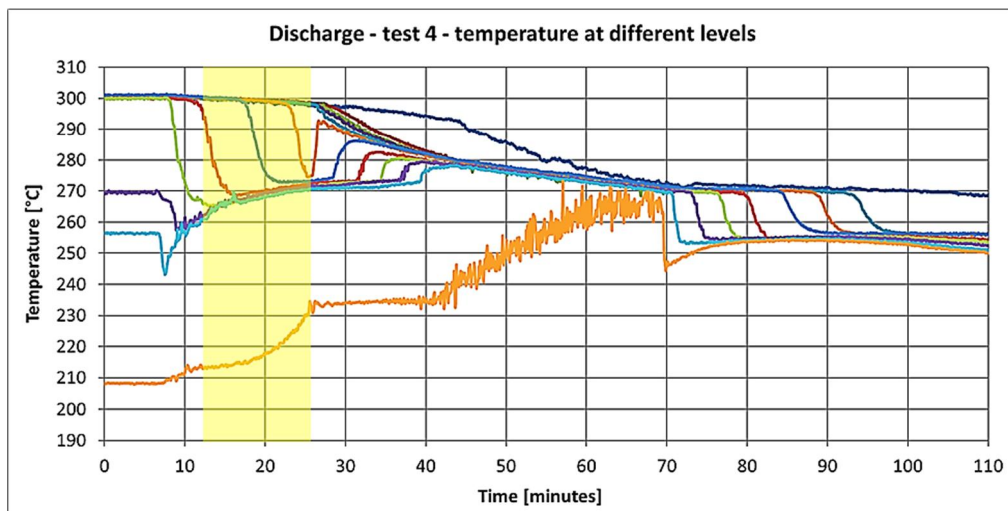
Other Results: Charge Test 1.1



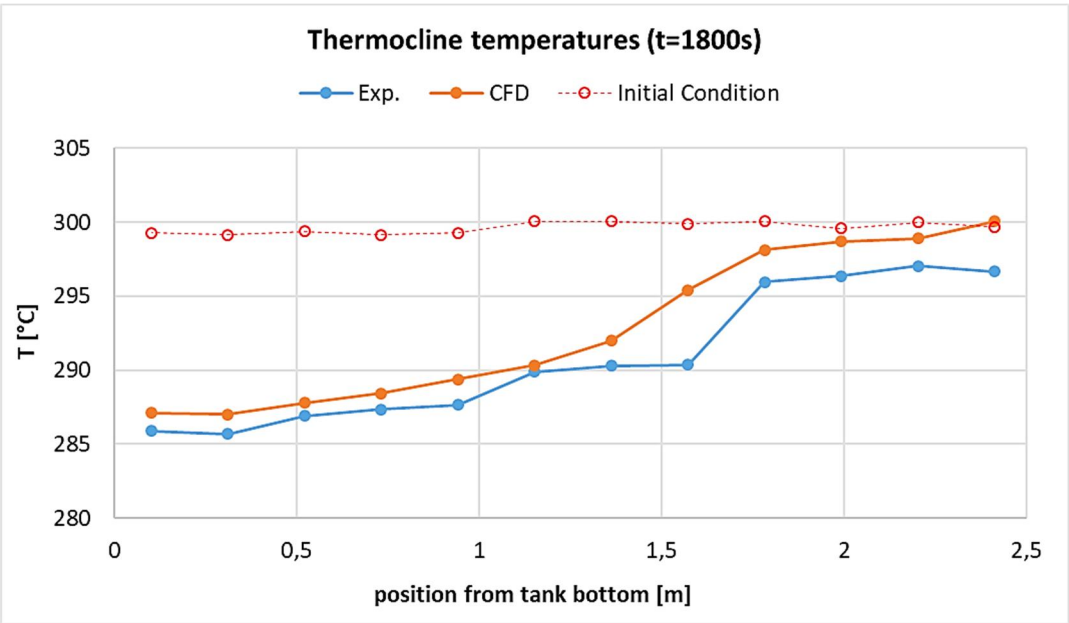
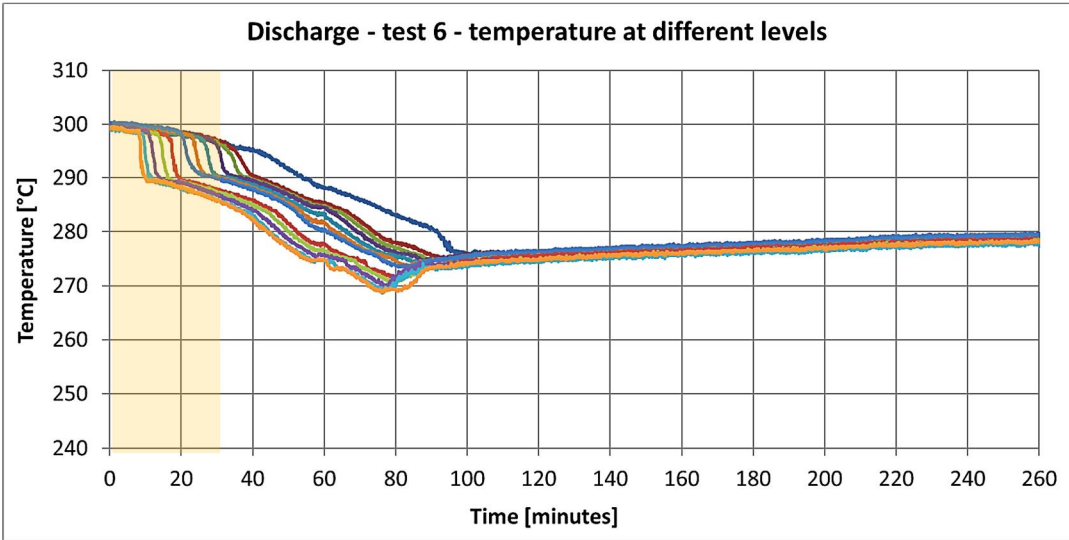
Other Results: Charge Test 1.2



Other Results: Discharge Test 4



Other Results: Discharge Test 6



References

- [1] [Online]. Available: <https://www.orc-plus.eu/>. [Accessed 26 10 2020].
- [2] T. Zhongchao, Air Pollution and Greenhouse Gases, Singapore: Springer, 2014.
- [3] IEA, “World Energy Outlook”, 2018. All rights reserved.
- [4] IEA, “Renewables 2019 - Analysis and Forecast to 2024”, 2019. All rights reserved.
- [5] World Energy Council, “World Energy Resources: Solar”, 2013.
- [6] P. Denholm, M. O'Connell, G. Brinkman and J. Jorgenson, “Overgenerations from Solar Energy in California: A Field guide to the Duck Chart”, NREL, Denver, 2015.
- [7] E. E. (Stathis) Michaelides, Alternative Energy Sources, Berlin: Springer, 2012.
- [8] C. W. Gellings, “The Concept of Demand-Side Management for Electric Utilities” *Proceedings of the IEEE*, vol. 73, no. 10, pp. 1468-1470, 1985.
- [9] J. Jorgenson, P. Denholm and M. Mehos, “Estimating the Value of Utility-Scale Solar Technologies in California under a 40% Renewable Portfolio Scenario”, NREL, Denver, 2014.
- [10] K. Lovegrove and W. Stein, Concentrating Solar Power Technology: Principles, Developments and Applications, Elsevier Science & Technology, 2012.
- [11] SolarPACES, Greenpeace, ESTELA, “Solar Thermal Electricity Global Outlook 2016”, Greenpeace International.
- [12] IRENA, “The Power to Change: Solar and Wind Cost Reduction Potential to 2025”, 2016.
- [13] R. Bradshaw and R. Carling, “A Review of the Chemical and Physical Properties of Molten Salts Alkali Nitrate Salts and their Effect on Materials Used for Solar Central Receivers” *Proceedings of The Electrochemical Society*, vol. 7, pp. 959-969, 1987.

- [14] D. Laing and D. Lehmann, “Concrete Storage for Solar Thermal Power Plants and Industrial Process Heat” in *3rd International Renewable Energy Storage Conference*, Berlin, 2008.
- [15] G. Giannuzzi, R. Liberatore, D. Mele, G. Mazzucco, G. Xotta, V. A. Salomoni, C. E. Majorana and R. Di Maggio, “Experimental Campaign and Numerical Analysis of Thermal Storage Concrete Modules” *Solar Energy*, vol. 157, pp. 596-602, 2017.
- [16] A. Pizzolato, F. Donato, V. Verda and M. Santarelli, “CFD-based reduced model for the simulation of the thermocline thermal energy storage systems” *Applied Thermal Engineering*, vol. 76, pp. 391-399, 2015.
- [17] M. A. Rosen, “The exergy of stratified thermal energy storages” *Solar Energy*, vol. 71, no. 3, pp. 173-185, 2001.
- [18] S. Afrin, V. Kumar, D. Bharathan, G. C. Glatzmaier and Z. Ma, “Computational Analysis of a Pipe Flow Distributor for a Thermocline Based Thermal Energy Storage System” *Journal of Solar Energy Engineering*, vol. 136, pp. 1-6, 2014.
- [19] W. Gaggioli, F. Fabrizi, F. Fontana, L. Rinaldi and P. Tarquini, “An innovative concept of a thermal energy storage system based on a single tank configuration using stratified molten salts as both heat storage medium and heat transfer fluid, and with an integrated steam generator” *Energy Procedia*, vol. 49, pp. 780-789, 2014.
- [20] L. Rinaldi, F. Fabrizi, A. Alemberti, W. Gaggioli, S. Aliotta, A. Barbensi and P. Tarquini, “Thermal-Energy-Storage Tank with Integrated Steam Generator”. Patent WO 2012/080970 A2, 21 June 2012.
- [21] M. Capocelli, A. Caputo, M. De Falco, D. Mazzei and V. Piemonte, “Two-Channels Thermal Energy Storage Tank: Experiments and Short-Cut Modelling” *International Journal of Energy and Environmental Engineering*, vol. 11, no. 10, pp. 923-927, 2017.
- [22] A. Giaconia, F. Montagnino, F. Paredes, F. Donato, G. Caputo and D. Mazzei, “Co-generation and Innovative Heat Storage System in Small-Medium CSP Plants for Distributed Energy Production” in *AIP Conference Proceedings*, 2016.

-
- [23] V. Russo, D. Mazzei and R. Liberatore, “Thermal energy storage with integrated heat exchangers using stratified molten salts system for 1 MWe CSP” in *AIP Conference Proceedings 2033*, 2018.
- [24] W. Gaggioli, R. Liberatore, P. Di Ascenzi, D. Mazzei and V. Russo, “Experimental Test of Characterization of an Innovative Thermal Energy Storage System Based on Low Melting Molten Salt Thermocline Tank Integrated with an Oil Exchanger” in *SolarPaces 2019*, in Review (2020).
- [25] J. Ferziger and M. Peric, *Computational Methods for Fluid Dynamics*, Berlin: Springer, 2002.
- [26] [Online]. Available:
<https://www.plm.automation.siemens.com/global/it/products/simcenter/STAR-CCM.html>. [Accessed 22 11 2020].
- [27] H. Versteeg and W. Malalasekera, *An Introduction to Computational Fluid Dynamics - The finite volume method*, Pearson Education Limited, 2007.
- [28] E. Rivas, E. Rojas, R. Bayon, W. Gaggioli, L. Rinaldi and F. Fabrizi, “CFD model of a molten salt tank with integrated steam generator” *Energy Procedia*, vol. 49, pp. 956-964, 2014.
- [29] F. P. Incropera, T. L. Bergman, A. S. Lavine and D. P. Dewitt, *Introduction to Heat Transfer - sixth edition*, John Wiley & Sons, 2011.
- [30] P. S. Purandare, M. M. Lele and R. K. Gupta, “Investigation on thermal analysis of conical coil heat exchanger” *International Journal of Heat and Mass Transfer*, vol. 90, pp. 1188-1196, 2015.
- [31] “Metheorological archive - IlMeteo.it,” [Online]. Available:
<https://www.ilmeteo.it/portale/archivio-meteo/Roma/2019/Gennaio>. [Accessed 11 11 2020].
- [32] R. Shah, “A Correlation for Laminar Hydrodynamic Entry Length Solutions for Circular and Noncircular Ducts” *Journal of Fluids Engineering*, vol. 100, pp. 177-179, 1978.

- [33] B. R. Munson, T. H. Okiishi, W. W. Huebsch and A. P. Rothmayer, *Fundamentals of Fluid Mechanics* - 7th Edition, John Wiley & Sons, 2013.
- [34] A. Cammi, M. Cauzzi, L. Luzzi and A. Pini, “DYNASTY: an experimental loop for the study of natural circulation within internally heated fluids” in *12th International Conference on Heat Transfer, Fluid Mechanics and Thermodynamics*, 2016.
- [35] F. Fanale, Development and assessment of Computational Fluid Dynamics models for the study of natural circulation dynamics, Milan: Politecnico di Milano - Master Thesis, 2015.
- [36] K. Lovegrove , J. Rutovitz, G. James, M. Watt, D. Leitch, J. Wyder and A. Ngo, “Comparison of Dispatchable Renewable Electricity Options”, 2018.
- [37] SCHOTT, “SCHOTT Solar,” [Online]. Available: <https://www.us.schott.com/csp/english/parabolic-through-technology.html>. [Accessed 02 11 2020].
- [38] F. Avallone, “Modeling of a Thermocline Energy Storage: application to a Concentrating Solar Thermal Power plant”, Master Thesis, Politecnico di Milano, 2018.
- [39] A. Pizzolato, F. Donato, V. Verda, M. Santarelli and A. Sciacovelli, “CSP plants with thermocline thermal energy storage and integrated steam generator - Techno-economic modeling and design optimization” *Energy*, pp. 231-246, 2017.